

Relations between the characteristics of granular column collapses and resultant high-frequency seismic signals

Maxime Farin, Anne Mangeney, Julien de Rosny, Renaud Toussaint, Phuong-Thu Trinh

▶ **To cite this version:**

Maxime Farin, Anne Mangeney, Julien de Rosny, Renaud Toussaint, Phuong-Thu Trinh. Relations between the characteristics of granular column collapses and resultant high-frequency seismic signals. Journal of Geophysical Research: Earth Surface, 2019, 10.1029/2019JF005258 . insu-02333954

HAL Id: insu-02333954
https://insu.hal.science/insu-02333954

Submitted on 31 Oct 2019

HAL is a multi-disciplinary open access archive for the deposit and dissemination of scientific research documents, whether they are published or not. The documents may come from teaching and research institutions in France or abroad, or from public or private research centers.

L'archive ouverte pluridisciplinaire **HAL**, est destinée au dépôt et à la diffusion de documents scientifiques de niveau recherche, publiés ou non, émanant des établissements d'enseignement et de recherche français ou étrangers, des laboratoires publics ou privés.

Relations Between the Characteristics of Granular Column Collapses and that of the Generated High-frequency Seismic Signal

Maxime Farin[1,2*], Anne Mangeney[2,3], Julien de Rosny[1], Renaud Toussaint[4,5], and Phuong-Thu Trinh[6]

.

[1]Institut Langevin, ESPCI Paris, PSL Research University, CNRS, Paris, France
[2]Institut de Physique du Globe de Paris, Sorbonne Paris Cité, CNRS (UMR 7154), Paris, France
[3]ANGE team, CEREMA, Inria, Lab. J.-L. Lions, CNRS, Paris, France
[4]Institut de Physique du Globe de Strasbourg/EOST, CNRS, Strasbourg, France
[5] SFF PoreLab, The Njord Centre, Department of Physics, University of Oslo, Oslo, Norway
[6]Total SA, Pau, France

Key Points:

- = We conduct granular column collapse experiments with various initial conditions and seismic measurements.
- = Empirical scaling laws are established between the dynamics and seismic parameters.
- = The increase of radiated seismic energy with slope angle matches with the increase in particle agitation.

*Institut Langevin, ESPCI Paris, PSL Research University, CNRS, 1 rue Jussieu, Paris, France

Corresponding author: Maxime Farin, maxime.farin@espci.fr

Abstract

Deducing relations between the dynamic characteristics of landslides and rockfalls and the generated high-frequency (> 1 Hz) seismic signal is challenging. In order to get some insights into what relations could be tested in the field, we conduct laboratory experiments of granular column collapse on a rough inclined thin plate, for a large set of column masses, aspect ratios, particle diameters and slope angles. The dynamics of the granular flows is recorded using a high speed camera and the generated seismic signal is measured using piezoelectric accelerometers. Empirical scaling laws are established between the characteristics of the granular flows and deposits and that of the generated seismic signals. The radiated seismic energy scales with particle diameter as d^3, column mass as M, aspect ratio as $a^{1.1}$ and initial column height as H_0^2. The increase of the radiated seismic energy as slope angle increases correlates with a similar increase in particle agitation. We interpret that the discrepancy of our empirical scaling laws with relations reported in the field can be explained by the complex influence of the substrate on seismic signal and the difference of flow initiation in both cases. However, our empirical scaling laws allow us to determine which flow parameters could be inferred from a given seismic characteristic in the field. In particular, by assuming the flow average speed is known, we show that we can retrieve parameters d, a and M within a factor of two from the seismic signal.

1 Introduction

Over the last two decades, seismic signals generated by granular flows (e.g. landslides, debris flows and rockfalls) have been more and more investigated, as a useful complementary tool to sparse visual observations, in order to detect flows and deduce informations about their localization and dynamics [e.g., *Arattano*, 2000; *Brodsky et al.*, 2003; *Suriñach et al.*, 2005; *Huang et al.*, 2007; *Dammeier et al.*, 2011; *Hibert et al.*, 2014a, 2017a,b; *Kean et al.*, 2015; *Zhao et al.*, 2015; *Pérez-Guillén et al.*, 2016; *Yamada et al.*, 2016; *Lai et al.*, 2018].

The high-frequency content (> 1 Hz) of the seismic signal is likely mostly generated by the numerous impacts of the particles composing the granular flows [*Huang et al.*, 2007; *Hsu et al.*, 2014; *Hibert et al.*, 2017c; *Farin et al.*, 2018, 2019]. An important parameter that may control high-frequency seismic amplitude is the fluctuating speed of

the particles, that is a measurement of the state of agitation of particles [often referred to as 'granular temperature', e.g. *Andreotti et al.*, 2013; *Delannay et al.*, 2017]. Fluctuating speed of the particle controls the rate of particle impacts [*Andreotti et al.*, 2013] and most probably the impact forces imparted by particles at the bed of granular flows [*Farin et al.*, 2019]. Therefore, the high-frequency signal is suspected to contain quantitative informations about characteristics of a granular flow and of the particles composing it, such as the size of the particles, the flowing volume (i.e. number of particles available to impact the bed) and the flow momentum (i.e. speed of the particles).

Only a few field studies could establish analytical scaling laws relating the flow parameters to the characteristics of the high-frequency seismic signal. The generally observed trend is that the maximum seismic amplitude A_{max} and absolute seismic energy W_{el} of the radiated seismic signal increases with the flow volume V, or particle mass/diameter in the case of individual block release [*Norris*, 1994; *Dammeier et al.*, 2011; *Hibert et al.*, 2011, 2017c; *Yamada et al.*, 2012; *Farin et al.*, 2015]. However, the reported empirical scaling laws relating these parameters seem to slightly depend on the investigated landslide site. For example, *Norris* [1994] and *Yamada et al.* [2012] noted that the maximum seismic amplitude A_{max} is proportional to the flow volume V for large landslides, while *Hibert et al.* [2011] rather reported a proportionality between the seismic energy W_{el} ($\propto A_{max}^2$) generated by rockfalls and their volume V for small rockfalls that occurred in the Dolomieu crater of the Piton de la Fournaise volcano, Reunion Island. In contrast, a more complex empirical relationship $V \propto t_s^{1.0368} EA^{-0.1248} A_{max}^{1.1446}$ with t_s, the flow duration and EA, the seismic envelope area, was found by *Dammeier et al.* [2011] using a statistical approach for 20 rockfall events. *Hibert et al.* [2017a] observed a good temporal correlation between the modulus of the momentum of the flow and the amplitude of the smoothed envelope of the seismic signal in the frequency range 3 to 10 Hz, for twelve worldwide large landslides. Moreover, they showed that the maximum seismic amplitude is proportional to the flow momentum. In the case of individual rock blocks impacts on a steep slope, the best fit to the seismic data shows a dependence of the radiated seismic energy W_{el} to the particle mass m and impact speed v_z as $mv_z^{0.5}$ [*Farin et al.*, 2015] or $mv_z^{13/5}$ [*Hibert et al.*, 2017c], based on analytical scaling laws for a sphere impacting a thick block established by *Farin et al.* [2015].

Most studies on the high-frequency seismic signal generated by granular flows were only able to observe a relative change in the seismic signal amplitude with a relative vari-

ation of a flow characteristic, if the other flow characteristics remain approximately constant [e.g. *Arattano*, 2000; *Huang et al.*, 2007; *Suriñach et al.*, 2005; *Burtin et al.*, 2009; *Kean et al.*, 2015]. For example, *Huang et al.* [2007] noted that the frequency of the seismic signal generated by debris flows decreases when the diameter of the involved particles increases. By comparing the seismic power generated by successive debris flows in the same channel, *Kean et al.* [2015] related the increase of seismic power between two debris flows to the decrease of the thickness of the underlying erodible sediment bed. Establishing clear quantitative scaling relations between the generated high-frequency seismic signal and flow parameters is difficult in the field because of numerous yet unparsed complexities. First, flows are heterogeneous, partly due to particle segregation [*Iverson*, 1997; *Kean et al.*, 2015], make it challenging to deduce one flow parameter (flow thickness, speed or particle diameter) from one seismic measurement. Then, irregularities in the bed topography such as turns and bumps and the presence of an erodible bed can cause a sudden increase or decrease in seismic amplitude along the flow path [*Favreau et al.*, 2010; *Allstadt*, 2013; *Moretti et al.*, 2015; *Kean et al.*, 2015; *Bachelet et al.*, 2018a]. In addition to the flow parameters, complex path effects (e.g. attenuation, dispersion of seismic wave), due to the heterogeneity of the ground, have a strong impact on the amplitude of the observed seismic signal [*Aki and Richards*, 1980]. Finally, visual observations of the dynamics of gravitational instabilities are rare due to the dangerousness and unpredictability of these events, which makes it harder to interpret the observed seismic amplitudes.

Most of these complexities are not present in acoustically monitored laboratory experiments of granular flows. Such experiments offer a convenient way to investigate the individual effect of each flow parameter on the generated seismic signal by varying one parameter while fixing the others. The dynamics of granular flows and the effect of the parameters of a released granular column on its runout distance has been extensively investigated in the laboratory during the past few decades [see e.g. *GdR Midi*, 2004; *Andreotti et al.*, 2013; *Delannay et al.*, 2017, for review]. In particular, authors reported that the runout distance r_f of granular flow is proportional to the initial height H_0 of the released granular column, regardless of the other flow parameters (volume, initial aspect ratio (i.e. height over length of the column) and particle shape, diameter and material) [e.g. *Balmforth and Kerswell*, 2005; *Lube et al.*, 2005; *Siavoshi and Kudrolli*, 2005; *Hogg*, 2007; *Mangeney et al.*, 2010; *Lube et al.*, 2011; *Farin et al.*, 2014]. While r_f can be uniquely

determined by H_0 for horizontal flows, *Mangeney et al.* [2010] showed analytically that r_f also increases with slope angle θ as

$$r_f \propto \frac{H_0}{\tan\delta - \tan\theta}, \quad (1)$$

where δ is the friction angle of the granular material. This scaling law has been validated for granular flows with a variety of volumes and aspect ratios (i.e. initial height over length of the granular column) for moderate slope angles $\theta < 15°$ [*Farin et al.*, 2014]. However, for higher slope angles $\theta > 15°$, the scaling law does not match the data as well [*Farin et al.*, 2014]. The origin of this discrepancy is thought to be related to a transition of the granular flow dynamics towards a regime with a long duration phase of slow flow velocity at the end of granular flow propagation at high slope angles θ, which extends significantly the runout distance of granular flows compared to more moderate slopes ($< 10°$) [*Mangeney et al.*, 2010; *Farin et al.*, 2014].

Recently, a few studies have investigated the boundary forces or seismic signal generated by particle impacts and granular flows using vibration sensors [e.g. *Huang et al.*, 2004; *Yohannes et al.*, 2012; *Hsu et al.*, 2014; *Barrière et al.*, 2015; *Farin et al.*, 2015; *Turkaya et al.*, 2015; *Taylor and Brodsky*, 2017; *Farin et al.*, 2018; *Bachelet et al.*, 2018a; *Turquet et al.*, 2018, 2019]. For example, *Yohannes et al.* [2012] and *Hsu et al.* [2014] measured the distribution of fluctuating forces at the base of dry and saturated granular flows in a rotating drum using force sensors. *Farin et al.* [2015] established analytical scaling laws relating the seismic energy radiated by particle impacts and the average frequency of the generated seismic signal to the particle mass and impact speed and validated these laws with laboratory experiments of impacts of particles of various diameters and materials. In particular, it was noted that the scaling laws have different coefficients when the impacts occur on thin plates or on thick blocks. The coefficients of these laws where also shown to vary when the impacts occur on a rough bed or on erodible beds of various thicknesses [*Bachelet et al.*, 2018a]. *Barrière et al.* [2015] measured the acoustic signal generated at the base of granular flows in a flume with a hydrophone attached under the flume and established an empirical scaling law relating the 50th percentile particle diameter D_{50} of the particle distribution in the granular flows to the maximum amplitude A_{max} and average frequency f_{mean} of the generated acoustic signal: $D_{50} \approx 5.0 \cdot 10^4 A_{max}^{0.39}/f_{mean}^{0.86}$. *Turkaya et al.* [2015] and *Turquet et al.* [2018, 2019] characterized the acoustic emissions of confined granular material in Hele-Shaw cells during shear and compaction caused by internal gas flow. Finally, *Taylor and Brodsky* [2017] conducted gran-

ular shearing experiments under constant confining pressure in a torsional rheometer on which a piezoelectric accelerometer was attached. They asserted that the acoustic energy radiated by the shearing was a proxy for the granular temperature and observed a linear relation between this acoustic energy and the inertial number, that quantifies the relative importance of inertia and confining stresses in the granular flow [*GdR Midi*, 2004]. Moreover, they showed that the ratio of acoustic energy over inertial number increases as the cube of the particle diameter.

In a previous paper, we performed seismically monitored 3D granular column collapse experiments on a rough inclined thin plate, with slope angle varying from the horizontal to 20° [*Farin et al.*, 2018]. The seismic signal generated by the granular flows was measured using piezoelectric accelerometers and the dynamics of the granular flows was recorded with a fast camera, allowing us to directly compare the seismic and dynamic properties of these flows. The main observations of this study were

1. The shapes of the temporal variation of the normalized radiated seismic energy and of the normalized potential energy lost by the granular flow match.
2. The shape of the seismic envelope changes when slope angle increases. We attributed this change of shape to the development of a different dynamic regime of the granular flows at high slope angles, from a dense flow to a more agitated and dilute flow. In both of these granular regimes, the motion of particles is ruled by collisions between themselves and with the bed [inertial flows, see *Andreotti et al.*, 2013]. Within the dense flow, the rate of particle impacts is high but particle have low relative speeds. In contrast, in the dilute regime, observed at the flow front with a cloud of particles rebounding high above the bed (saltating front), the rate of particle impacts is lower but particles impart stronger forces on the bed, potentially generating higher seismic energy than in the flow rear.
3. The amplitude of the seismic envelope seems more related with the speed of the flow center-of-mass in the direction normal to the plate during the rise phase (acceleration phase of the flow). In contrast, the maximum seismic amplitude matches with the speed of the flow center-of-mass in the downslope direction at the end of the propagation of the flow, when flow motion direction is mostly downslope.

However, these experiments were performed using particles of only one diameter $d = 2$ mm, and the released granular columns had only one mass $M = 77.4$ g and as-

pect ratio $a = 0.8$ (i.e. height over diameter of the column). The conclusions of this last paper may then only apply for this specific set of parameters. Therefore, in the present paper, we pursue the work initiated by *Farin et al.* [2018] by releasing 3D granular columns of various particle diameters d, masses M and aspect ratios a. Note that all particles have the same diameter in our experiments. The effect of various particle distributions, as well as the effect of a complex bed shape and presence of an erodible bed are not explicitly explored in this study but would be useful to investigate in future works to better understand the complexities encountered on the field that we mentioned earlier. The specific questions we would like to address are: (1) Are the observations of *Farin et al.* [2018] still valid for different particle diameters, column masses and aspect ratios? (2) Can we establish clear empirical scaling laws relating the absolute radiated seismic energy W_{el}, the seismic efficiency (ratio of W_{el} over total potential energy lost or over maximum kinetic energy) and the frequency of the generated seismic signal to the parameters of the released granular columns? Are these laws modified when the slope angle increases? In particular, does the radiated seismic energy depend on slope angle similarly as the runout distance (inversely proportional to $\tan\delta - \tan\theta$ as in equation (1))? Since the flow becomes more agitated as slope angle increases, it is interesting to correlate the increase of the radiated seismic energy with the increase of particle agitation in the saltating front. (3) How do the empirical scaling laws compare to previous field observations and to that established for a single particle impact? (4) Finally, what properties of granular flows (particle diameter, mass, speed) can we infer from each characteristic of the radiated seismic signal in the field?

The paper is organized as follows: In section 2, we present the experimental setup and define the investigated dynamics and seismic flow parameters. In section 3, we compare the dynamics of granular flows and the generated seismic signals for different flow parameters and we establish empirical scaling laws. The results are interpreted in section 4 and compared with observations for a single particle impact and in the field. Based on our observed scaling laws, we also discuss which flow properties are possible to deduce from high-frequency seismic signals in the field. Finally, section 5 presents the conclusions and perspectives.

2 Experimental Setup and Definition of Flow and Seismic Parameters

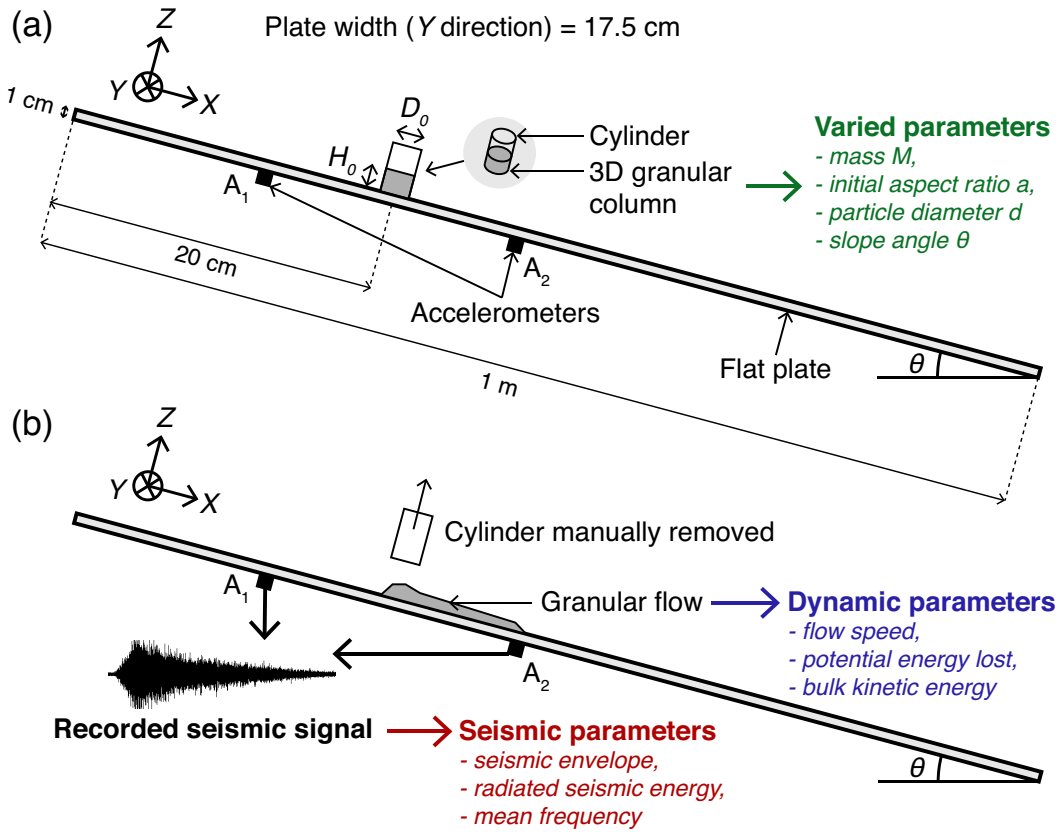
2.1 Experimental Setup

The experimental setup is the same as the one introduced by *Farin et al.* [2018] (Fig. 1). Cylindric granular columns with various initial conditions are suddenly released on a PMMA (Polymethyl methacrylate) plate of thickness $h = 1$ cm. The columns are composed of spherical steel particles of density 7800 kg m^{-3} and of same diameter d. The friction angle of the granular material is $\delta = 27°$. A layer of 2-mm steel beads is glued on the plate surface to create basal roughness and ensure the granular flows form a deposit on the plate when it is inclined. *Farin et al.* [2018] investigated only one column mass $M = 77.4$ g, initial aspect ratio $a = H_0/D_0 = 0.8$ (where H_0 and D_0 are the column's initial height and diameter) and particle diameter $d = 2$ mm for different slope angles $\theta = 0° - 20°$ on the resulting flow dynamics and generated seismic signal. In this paper, we conduct several series of experiments for which one parameter M, a, d and θ is varied while the others are fixed. Table 1 sums up the range of parameters investigated. Note that only the effect of the column mass M (for a fixed aspect ratio $a = 0.8$) and of the aspect ratio a (for a fixed mass $M = 70$ g) are investigated when the slope angle θ increases. An additional series of granular column collapse experiments is also conducted on a thick marble block in order to observe the influence of the substrate (thin plate or thick block) on the relations between seismic and initial columns parameters (see Appendix A:).

A video camera recording 500 frames per second is installed along the side of the granular flow in order to capture the flow dynamics. This recording speed is sufficient to track the motion of individual particles rebounding in front of the flow. In parallel, the seismic vibration generated by the granular flows is measured with using two mono-component piezoelectric accelerometers (type 8309, *Brüel & Kjaer*). The response of these sensors is flat between 1 Hz and 54 kHz. This experimental setup allows us to observe how the properties of the seismic signal (radiated seismic energy, seismic envelope, frequencies) are related to the dynamics and deposit characteristics of the granular flows (potential and kinetic energy, flow speed and acceleration, total flow duration and runout distance) for various initial conditions. Let us first define the dynamics and seismic parameters that we compare in the following sections.

Table 1. Characteristics of the 3D granular columns released on the PMMA plate. When various column initial heights H_0 are given, they correspond to the variation of either the mass M or the aspect ratio a.

d (mm)	M (g)	a (-)	H_0 (cm)	θ (°)
2	11.1, 30.9, 37.8, 53	0.4	0.79, 1.11, 1.18, 1.32	0
	16.6, 46.4, 56.7, 79.5	0.6	1.18, 1.67, 1.77, 2	
	22.2, 61.8, 75.6, 105.9, 246.5	0.8	1.58, 2.22, 2.36, 2.65, 3.52	
	27.7, 77.3, 94.5, 308.1	1	2, 2.78, 2.95, 4.4	
2	50	0.16, 0.38, 0.53, 0.65, 1.82	0.7, 1.25, 1.56, 1.8, 3.55	0
	70	0.22, 0.53, 0.74, 0.9	1, 1.75, 2.18, 2.5	
	90	0.28, 0.66, 0.95, 1.11	1.25, 2.2, 2.8, 3.2	
	110	0.36, 0.81, 1.12, 1.37	1.6, 2.7, 3.3, 3.8	
1, 1.58, 2, 2.38, 3.17	126 ± 0.3	0.4	1.76	0
	189 ± 0.3	0.6	2.64	
	100 ± 2	0.75	3	
	132.5 ± 0.2	1	3.31	
2	22.7, 64.4, 77.4, 107.7, 246.1	0.8	1.58, 2.22, 2.36, 2.65, 3.52	0, 5, 10, 15, 20
	70	0.23, 0.52, 0.72, 0.87	1, 1.72, 2.13, 2.42	



232 **Figure 1.** Schematic of the experimental setup (Modified from [*Farin et al.*, 2018]). (a) A
233 granular column is initially contained in a cylinder on a flat plate inclined at slope angle θ. The
234 granular column has an initial height H_0 and diameter D_0, a mass M and initial aspect ratio
235 $a = H_0/D_0$ and is composed of spherical steel particles of diameter d. (b) The cylinder is sud-
236 denly removed and the granular column spreads down the slope. The dynamics of the granular
237 flow (flow speed, potential energy lost, bulk kinetic energy) is recorded along the side using
238 a video camera and the seismic signal generated by the flow is measured by two piezoelectric
239 accelerometers (A_1 and A_2) attached to the bottom of the plate.

2.2 Dynamic Parameters

We deduce the dynamic parameters from the time evolution of the flow contour profile $H(X,t)$ evaluated from the successive pictures of the granular flows in the (X,Y,Z) frame linked to the plate (Fig. 2a).

The potential energy lost by the granular flow as a function of time t is

$$\Delta E_p(t) = E_p(t=0) - E_p(t), \tag{2}$$

with the potential energy $E_p(t)$ computed using the following expression demonstrated by *Farin et al.* [2018]

$$E_p(t) \simeq \frac{1.5}{2}\rho g D_0 \left(\frac{1}{2}\int_X H(X,t)^2 \cos\theta \mathrm{d}X - \int_X H(X,t) X \sin\theta \mathrm{d}X \right), \tag{3}$$

where $\rho = M/(\pi D_0^2 H_0/4) \simeq 4800$ kg m^{-3} is the average density of the granular flow, g is the gravitational acceleration and D_0 is the initial column diameter.

Since most of granular flow motion is in the plane $(X, Y=0, Z)$, we neglect flow motion in the Y-direction. The coordinates $(X^{COM}(t), Z^{COM}(t))$ of the flow center of mass are obtained by integration of the flow profile $H(X,t)$ along the X and Z-directions, respectively (see *Farin et al.* [2018] for details on the computations of these coordinates). Time derivation of these coordinates gives the bulk speeds $V_X^{COM}(t)$ and $V_Z^{COM}(t)$ in X and Z-directions and the total bulk speed $V_{tot}^{COM}(t) = \sqrt{V_X^{COM}(t)^2 + V_Z^{COM}(t)^2}$. The bulk kinetic energy $E_k(t)$ of the flow is then defined as

$$E_k(t) = \frac{1}{2} M V_{tot}^{COM}(t)^2, \tag{4}$$

and the total energy lost by the granular flow at time t is

$$E_{tot}(t) = \Delta E_p(t) + E_k(t) \tag{5}$$

It is unclear whether the high-frequency seismic amplitude generated by granular flows is more controlled by the motion of the center of mass or by the motion of the flow snout, which propagates faster (and thus is more energetic) than the flow rear. Therefore, we also measure the speed $V_{front}(t)$ of the front of the granular flows and that of the column's summit (towards the plate in the Z-direction) $V_{summit}(t)$.

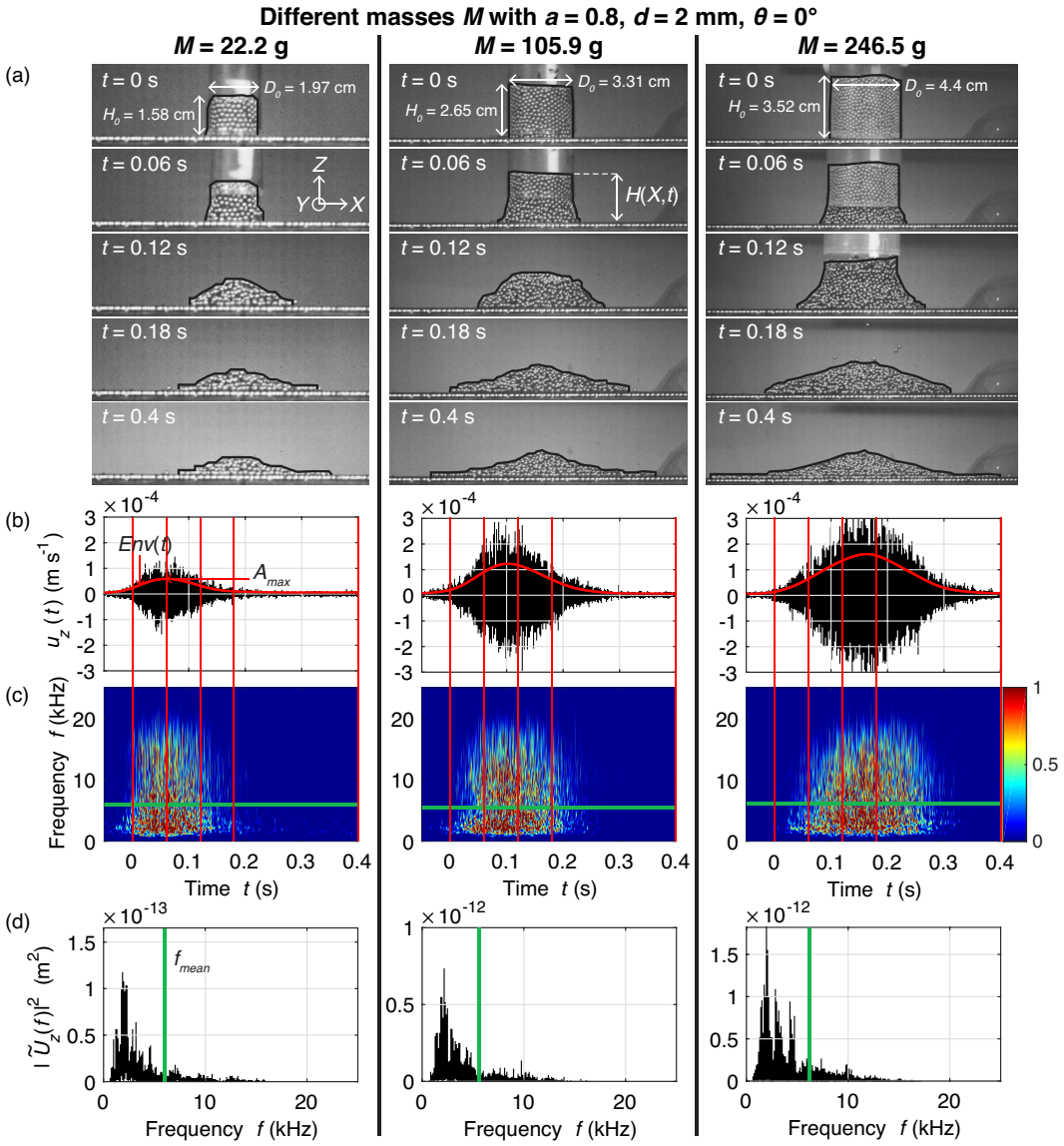


Figure 2. (a) Successive pictures of three horizontal ($\theta = 0^\circ$) 3D granular column collapse experiments with different masses $M = 22.2$ g, $M = 105.9$ g and $M = 246.5$ g, all with initial column aspect ratio $a = 0.8$ and particle diameter $d = 2$ mm. The black lines show the contours $H(X,t)$ of the granular flows that are used to compute the flow dynamic parameters. (b) Seismic signals (i.e. plate vibration speed $u_Z(t)$) generated by the granular flows as a function of time t. The red line represent the amplitude envelope, filtered below 5 Hz. (c) Spectrograms of the signals. Warmer colors mean more energy (normalized to 1). (d) Squared amplitude spectra $|\tilde{U}_Z(f)|^2$ of the seismic signals. The vertical red lines in panels (b) and (c) indicate the times of the pictures in (a) and the thick green line in panels (c) and (d) indicates the mean frequency f_{mean} of the signals.

2.3 Seismic Parameters

The two accelerometers attached to the plate measure the acceleration $a_Z(t)$ of the plate surface in the Z-direction generated by the granular flows. We integrate $a_Z(t)$ to obtain the speed $u_Z(t)$ of the plate vibration, that we call the 'seismic signal' in the following (Fig. 2b). *Farin et al.* [2018] showed that both accelerometers measure the same seismic amplitude because the seismic waves emitted by the granular flows are reflected many times off the boundaries of the plate and the radiated seismic energy is rapidly equipartitioned within the plate. We are therefore confident that an increase in the seismic amplitude reflect a change in the dynamics of the granular flows and not the fact that the flow gets closer to the accelerometer.

We characterize the seismic signal by its seismic envelope $Env(t)$ and its maximum value A_{max} (Fig. 2b). A Fourier transform of the seismic signal $u_Z(t)$ gives the spectrogram and the amplitude spectrum $|\tilde{U}_Z(f)|$ (Fig. 2cd). We characterize the amplitude spectrum with its average frequency defined as

$$f_{mean} = \frac{\int_0^{+\infty} |\tilde{U}_Z(f)| f \mathrm{d}f}{\int_0^{+\infty} |\tilde{U}_Z(f)| \mathrm{d}f}. \quad (6)$$

We choose to use the mean frequency rather than, for example, the maximum frequency of the spectrum because it averages the contributions of all of the particles impacting the bed during the granular flow. Indeed, each impact of the particles during the granular flow has a slightly different duration, which results in a slightly wider or less wide frequency spectrum. By taking the average frequency, we take the average of the frequency spectra of all impacts.

The seismic parameter we are most interested in is the absolute energy W_{el} radiated in the form of elastic waves by the granular flows because, in the field, this parameter does not depend on the distance between the source and the seismic station and can quantitatively be compared with the potential energy lost ΔE_p and the kinetic energy E_k of the granular flows [e.g. *Vilajosana et al.*, 2008; *Hibert et al.*, 2011; *Lévy et al.*, 2015; *Hibert et al.*, 2017c]. As discussed by *Farin et al.* [2018], the normal motion $u_Z(t)$ measured at one location of the plate surface is sufficient to evaluate $W_{el}(t)$. Indeed, in the frequency range of interest (1−20 kHz), the only mode excited in the plate is the flexural mode A_0 which has a displacement normal to the plate surface [*Royer and Dieulesaint*, 2000]. *Farin et al.* [2018] demonstrated a method to evaluate the radiated seismic energy $W_{el}(t)$ in this experimental context, which is different than classical techniques

used for rockfalls and landslides in the field [e.g. *Vilajosana et al.*, 2008; *Hibert et al.*, 2011; *Lévy et al.*, 2015; *Hibert et al.*, 2017c]

$$W_{el}(t) \approx \frac{\rho_p V_p}{\tau} \int_0^t u_Z(t')^2 \mathrm{d}t', \tag{7}$$

where $u_Z(t)$ is the seismic signal, ρ_p and V_p are the density and volume of the plate, respectively and τ is the characteristic time of energy dissipation in the plate, which depends on frequency [*Farin et al.*, 2016]. The total seismic energy radiated during the whole experiment is then $W_{el} = W_{el}(t_s)$, where t_s is the duration of the seismic signal.

3 Comparison of the Seismic and Dynamic Parameters

3.1 Description of the Seismic Signals

The seismic signals generated by the granular column collapses have an emergent rise and long decay (Fig. 2b, 3b and 4b) and compare well with seismic signals of landslides and rockfalls observed in the field [*Schneider et al.*, 2010; *Dammeier et al.*, 2011; *Hibert et al.*, 2011; *Moretti et al.*, 2012; *Hibert et al.*, 2014b; *Pérez-Guillén et al.*, 2016]. Similarly as was previously reported by *Farin et al.* [2018], on an horizontal slope the shape of the seismic envelope is symmetrical with respect to its maximum. As the slope angle θ increases, the duration of decay phase increases with respect to that of the rise phase because the flow takes a longer duration to decelerate as the importance of gravity increases over frictional forces. At high slope angles, the decay phase is much more elongated than the rise phase (for example compare Fig. 2b for $\theta = 0°$ with Fig. 3b for $\theta = 15°$). Interestingly, this dependence of the signal shape to slope angle is observed regardless of the column mass M or initial aspect ratio a (Fig. 2bc and 3bc for the mass M; see Appendix B: , Fig. B.1 and B.2 for the aspect ratio a). We think that this change of shape is related to a change of the flow regime from a dense flow to a diluted and agitated flow, with a front of particles saltating on the bed which is not observed at small slope angles θ (see Fig. 3a for $t > 0.18$ s) [*Farin et al.*, 2018]. Regardless of the flow parameters, the granular flows generate a signal of frequencies between 1 kHz and 20 kHz (Fig. 2cd, 3cd and 4cd). Effects of flow parameters on the average frequency f_{mean} is discussed in section 3.3.

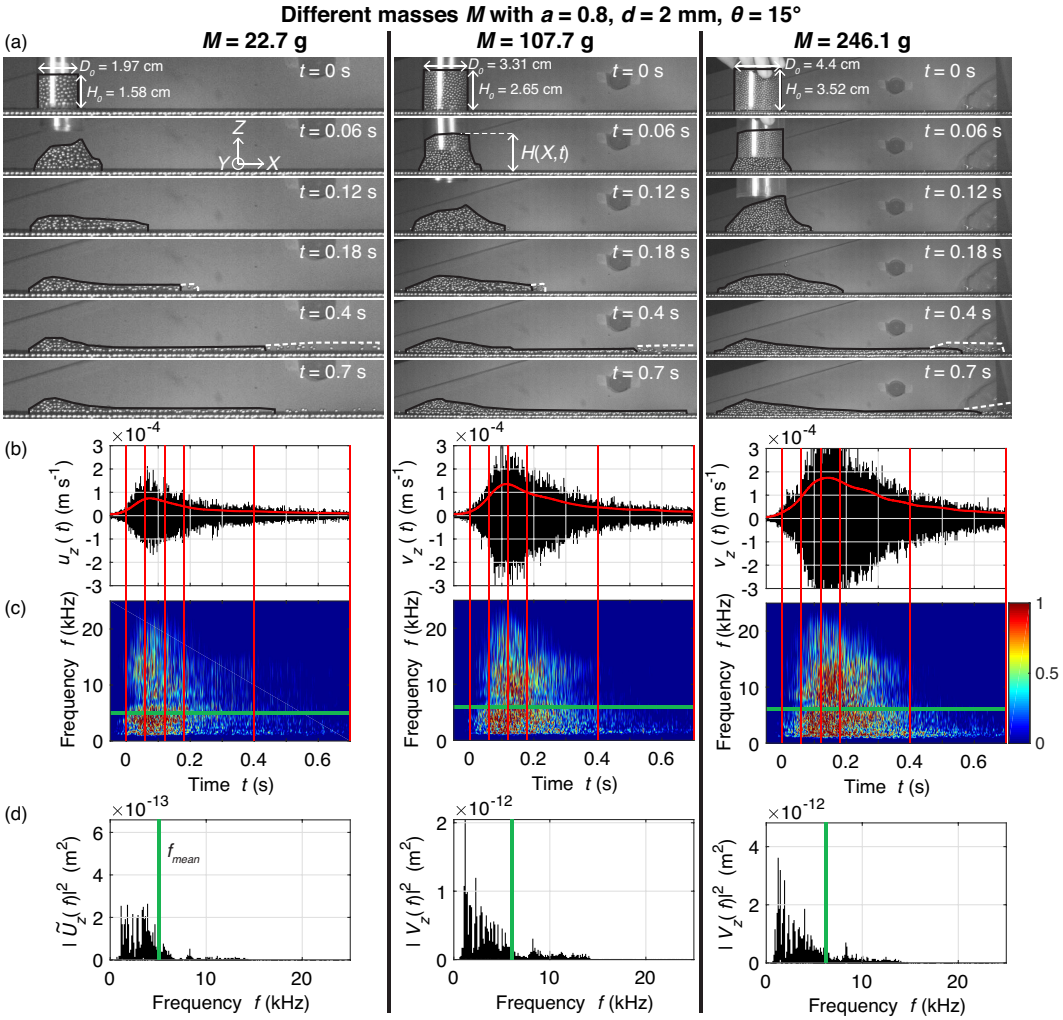


Figure 3. Same as Fig. 2 but when the plate is inclined at slope angle $\theta = 15°$. The white dashed line in (a) shows the contour of the assembly of saltating particles at the front of the granular flow.

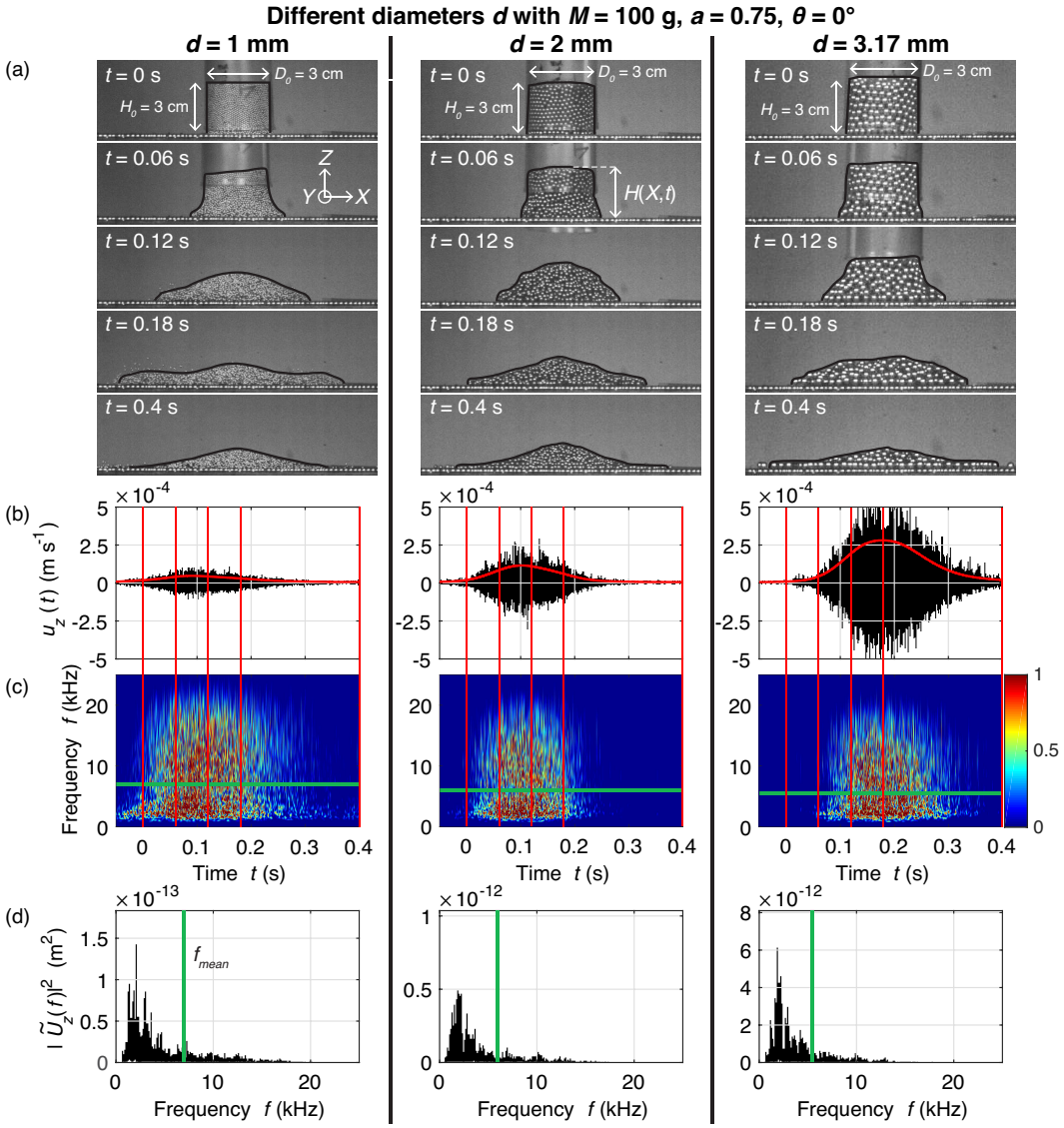


Figure 4. (a) Successive pictures of three horizontal ($\theta = 0°$) granular column collapse experiments with different particle diameter $d = 1$ mm, $d = 2$ mm and $d = 3.17$ mm, all with initial column aspect ratio $a = 0.75$ and mass $M = 100$ g. The black lines show the contours $H(X,t)$ of the granular flows that are used to compute the flow dynamic parameters. (b) Seismic signals (i.e. plate vibration speed $u_Z(t)$) generated by the granular flows as a function of time t. The red line represent the amplitude envelope, filtered below 5 Hz. (c) Spectrograms of the signals. Warmer colors mean more energy (normalized to 1). (d) Squared amplitude spectra $|\tilde{U}_Z(f)|^2$ of the seismic signals. The vertical red lines in panels (b) and (c) indicate the times of the pictures in (a) and the thick green line in panels (c) and (d) indicates the mean frequency f_{mean} of the signals.

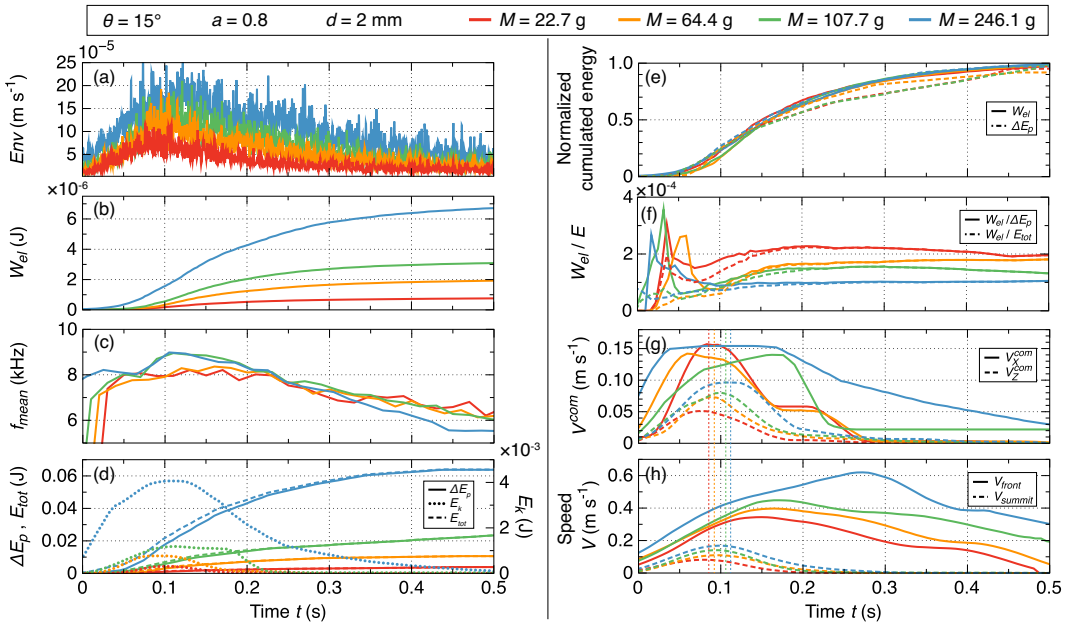


Figure 5. Comparison of the dynamics of granular flows with the generated seismic signal for $\theta = 15°$, $a = 0.8$, $d = 2$ mm and different column masses M (different colors). (a) Envelope $Env(t)$ of the seismic signal filtered below 100 Hz. (b) Radiated seismic energy $W_{el}(t)$. (c) Mean frequency f_{mean}. (d) Potential energy lost ΔE_p, kinetic energy E_k and total energy $E_{tot} = \Delta E_p + E_k$. (e) Normalized cumulated radiated seismic energy $W_{el}(t)$ and potential energy lost ΔE_p. (f) Ratio of the radiated seismic energy over the potential energy lost and the total energy lost. (g) Speeds V_X^{COM} and V_Z^{COM} of the flow center-of-mass in the X and Z-directions, respectively. (h) Speed V_{front} and V_{summit} of the flow front (in X-direction) and of the flow summit (in Z-direction). In panels (g) and (h), the vertical dashed lines indicate the maximum of the envelope $Env(t)$ of the seismic signal.

3.2 Temporal Comparison of Flow Dynamics with Seismic Signal

The temporal variation of the seismic and dynamic characteristics is compared for different masses M at slope angle $\theta = 15°$ in Fig. 5 and for different particle diameters d at $\theta = 0°$ in Fig. 6 (see Appendix B: , Fig. B.3 for different masses M at $\theta = 0°$ and Fig. B.4 and B.5 for different aspect ratios a). The quantitative influence of these parameters on seismic signal characteristics is discussed in the next section 3.3.

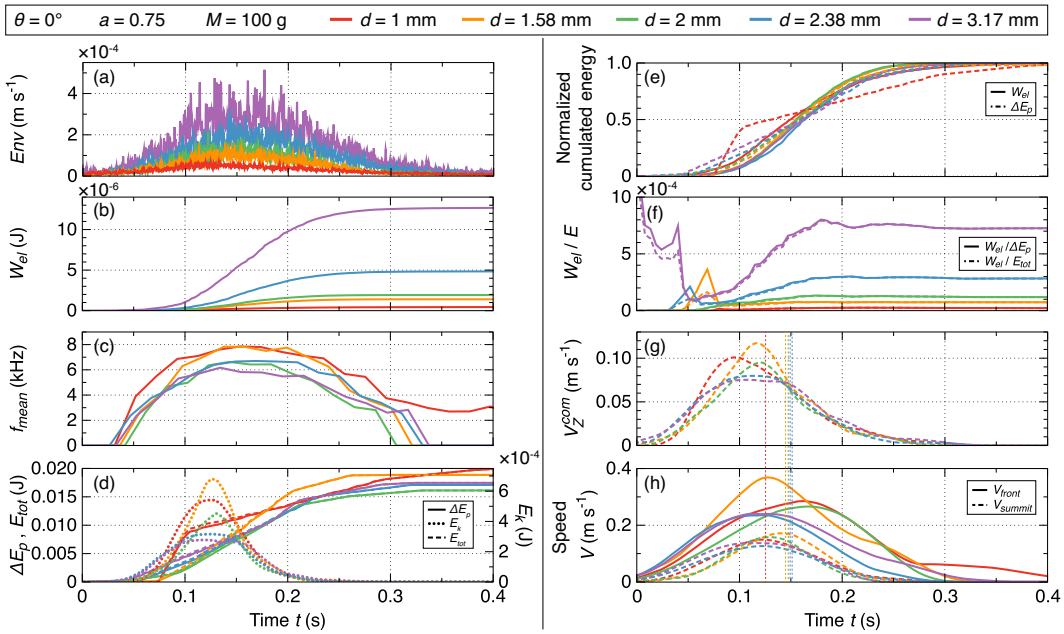


Figure 6. Same as Fig. B.3 but for $\theta = 0°$, $a = 0.75$, $M = 100$ g and different particle diameters d (different colors).

The observations of *Farin et al.* [2018] for one set of parameters M, a and d and different slope angles θ remain true for various masses M, aspect ratios a and particle diameters d. Mainly:

1. The maximum seismic amplitude coincides well with the maximum flow speed in the Z-direction (e.g. compare maximum $Env(t)$, indicated by vertical dashed lines, with the speeds V_Z^{COM} and V_{summit} for Fig. 5agh). In contrast, the seismic amplitude does not match with flow motion in the X-direction during the rise phase but starts depending on motion in this direction during the deceleration phase when flow motion in the Z-direction has stopped (e.g. compare maximum $Env(t)$ with the speeds V_X^{COM} and V_{front} for 5agh).
2. The time variation of the radiated seismic energy $W_{el}(t)$ and the potential energy lost $\Delta E_p(t)$ is similar and their normalized profiles match well (Fig. 5bde and 6bde). Same observations can be made when comparing W_{el} with the total energy lost E_{tot} because the bulk kinetic energy E_k is much smaller than the potential energy lost $\Delta E_p(t)$, so that $E_{tot} \approx \Delta E_p$ (Fig. 5d and 6d).

3. The seismic efficiency (i.e. the ratio $W_{el}(t)/\Delta E_p(t)$ or $W_{el}(t)/E_{tot}(t)$) is difficult to evaluate in the rise phase because energies are small but it tends towards a constant value in the decay phase (Fig. 5f and 6f). In the next section, we inspect how this final value (at the end of the flow) quantitatively changes when flow parameters vary.
4. The increase of the duration of the flow deceleration phase when the slope angle θ increases is visible in the shape of the seismic signal amplitude, energy and mean frequency and of the normalized curves of $W_{el}(t)$ and $\Delta E_p(t)$ (with a much longer decay phase than for $\theta = 0°$, Fig. 5abce).

3.3 Influence of Granular Column Initial Parameters

We now discuss how the particle diameter d, column mass M, initial aspect ratio a and slope angle θ quantitatively affect the total radiated seismic energy W_{el} (for the whole signal duration t_s), the ratio of this energy over the total potential energy lost $\Delta E_p = \Delta E_p(t_s)$, and over the maximum kinetic energy $E_k = \frac{1}{2} M \max(V_{tot}^{COM})^2$ and the mean frequency f_{mean} of the total seismic signal (Fig. 7). Data in Fig. 7 are fitted by power laws $Y = bX^c$, and parameters b and c are given in Table 2.

The radiated seismic energy W_{el} strongly depends on particle diameter as d^3, regardless of the column's mass M and aspect ratio a (Fig. 7a). In contrast, W_{el} increases approximatively linearly with column's mass as $M^{1.0}$ and column's initial aspect ratio as $a^{1.1}$ (Fig. 7ei). Increasing the particle diameter d while keeping all other parameters (M, a, θ) unchanged does not affect the bulk flow dynamics (i.e. ΔE_p, E_k and flow bulk speeds), but it only increases the radiated seismic energy W_{el} (Fig. 6bdgh). Consequently, the power 3 dependence in particle diameter d is conserved for the ratio of radiated seismic energy W_{el} over potential energy lost ΔE_p and maximum kinetic energy E_k (Fig. 7bc). On the contrary, varying the column's mass M and aspect ratio a affect the bulk flow dynamics (Fig. 5bdgh and Appendix B:). Both ΔE_p and E_k appear to depend on flow mass as about $M^{1.3}$, so that ratios $W_{el}/\Delta E_p$ and W_{el}/E_k are approximately proportional to $M^{-0.3}$ (Fig. 7fg). The dependence of W_{el} and ΔE_p on aspect ratio a is approximately the same, so that the ratio $W_{el}/\Delta E_p$ does not depend on a (Fig. 7j). In contrast, the kinetic energy E_k strongly depends on aspect ratio a, at least at power 2.3, because higher a imply higher heights of fall of the particles and higher maximum flow speeds, and consequently $W_{el}/E_k \propto a^{-1.3}$ (Fig. 7k). We have strong uncertainties ($\sim$

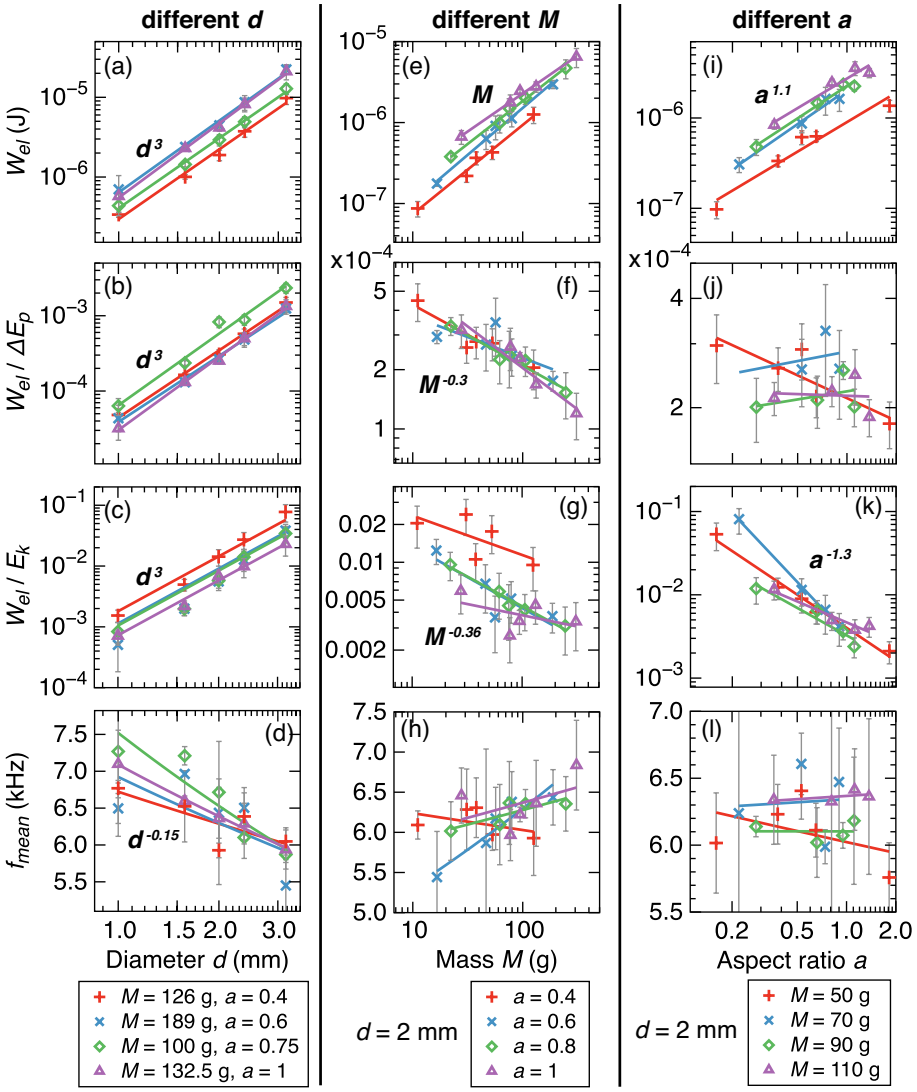


Figure 7. Seismic parameters as a function of the granular column parameters for the experiments on the PMMA thin plate. (a),(e),(i) Radiated seismic energy W_{el}, (b),(f),(j) Ratio of W_{el} over the potential energy lost ΔE_p, (c),(g),(k) Ratio of W_{el} over the total kinetic energy ΔE_k, (d),(h),(l) Mean frequency f_{mean} of the seismic signal for (a) to (d) different particle diameter d for various couples of fixed column mass M and initial aspect ratios a, (e) to (h) different masses M for $d = 2$ mm and fixed aspect ratios a and (i) to (l) different aspect ratios a for $d = 2$ mm and fixed masses M. Data are fitted by power laws (full lines). The power law is indicated when a tendency is observed (see Table 2 for details).

Table 2. Power laws $Y = bX^c$ used to fit the data in Fig. 7 and uncertainties Δb and Δc on parameters b and c. Coefficients are given in S.I. units.

Y	=	bX^c	Δb	Δc	R^2
		$4.7 \cdot 10^2 d^{3.0}$	$\pm 1.5 \cdot 10^2$	± 0.1	0.99
W_{el}	=	$2.1 \cdot 10^{-5} M^{1.06}$	$\pm 1.7 \cdot 10^{-5}$	± 0.09	0.99
		$2.0 \cdot 10^{-6} a^{1.14}$	$\pm 0.8 \cdot 10^{-6}$	± 0.08	0.96
		$4.4 \cdot 10^4 d^{3.0}$	$\pm 1.5 \cdot 10^4$	± 0.2	0.99
$W_{el}/\Delta E_p$	=	$1.2 \cdot 10^{-4} M^{-0.3}$	$\pm 4.3 \cdot 10^{-5}$	± 0.09	0.82
		$2.3 \cdot 10^{-4} a^{-0.01}$	$\pm 0.3 \cdot 10^{-4}$	± 0.13	0.24
		$7.7 \cdot 10^5 d^{3.0}$	$\pm 3.8 \cdot 10^5$	± 0.2	0.95
W_{el}/E_k	=	$2.6 \cdot 10^{-2} M^{-0.36}$	$\pm 1.3 \cdot 10^{-2}$	± 0.15	0.6
		$3.8 \cdot 10^{-3} a^{-1.3}$	$\pm 0.6 \cdot 10^{-3}$	± 0.5	0.96
		$2.55 \cdot 10^3 d^{-0.15}$	± 100	± 0.04	0.71
f_{mean}	=	$6.6 M^{0.027}$	± 0.96	± 0.036	0.48
		$6.2 a^{-0.002}$	± 0.2	± 0.012	0.37

20%) on the data of the mean frequency f_{mean}, which makes it difficult to draw conclusions from these data, especially as a function of M and a (Fig. 7dhl). The variation of f_{mean} as a function of the particle diameter d is slightly larger than the error bars and we can note a small decrease of f_{mean} as $d^{-0.15}$.

The power in the scaling laws as a function of mass M and aspect ratio a is only sightly modified when the slope angle θ increases (Fig. 8). The apparent independence of $W_{el}/\Delta E_p$ on mass M for $\theta = 20°$ (purple line, Fig. 8b) may be due to the fact that we underestimated ΔE_p for the large mass $M = 246.5$ g since the front of the flow propagated outside of the camera view. Contrary to the power coefficient, the value of the proportionality coefficient in the scaling laws significantly changes as slope angle θ increases. Indeed, regardless of M and a, the radiated seismic energy W_{el} increases when the slope angle θ increases, but only after a critical slope angle θ, between 10° and 15° (Fig. 8ab and 9ab). The increase is stronger as θ approaches the friction angle $\delta = 27°$. We further discuss this dependence in section 4.1. The ratios $W_{el}/\Delta E_p$ and W_{el}/E_k globally decrease as slope angle θ increases until $\theta = 20°$ for which the ratios increase again

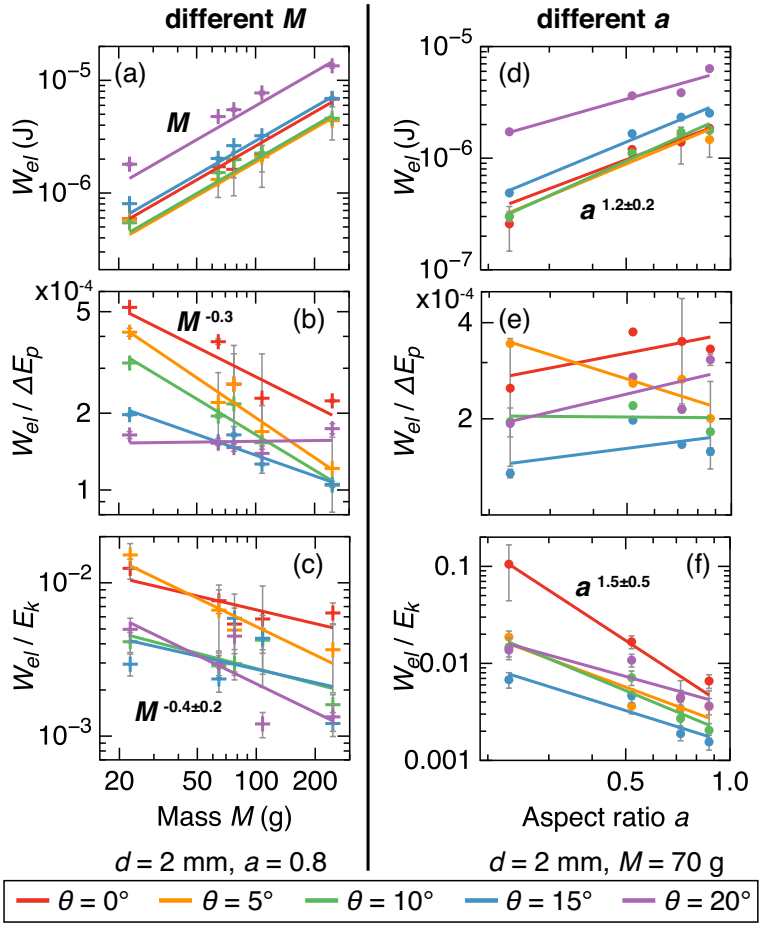
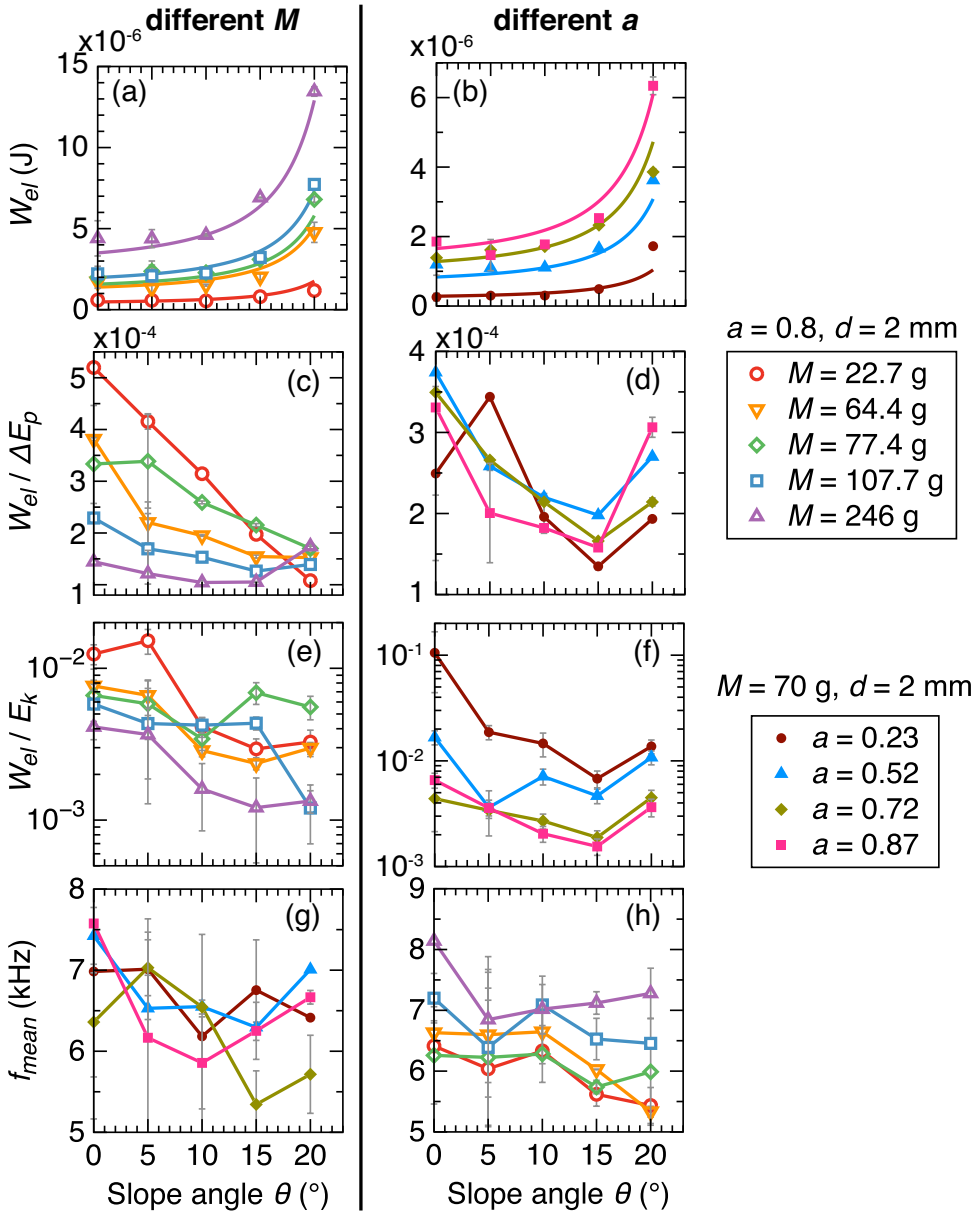


Figure 8. Influence of the slope angle θ (different colors) of the PMMA plate on the scaling laws of seismic parameters with mass M and aspect ratio a. (a),(d) Radiated seismic energy W_{el}, (b),(e) Energy ratio $W_{el}/\Delta E_p$ and (c),(f) Energy ratio W_{el}/E_k, for (a) to (c) $d = 2$ mm, $a = 0.8$ and different masses M and (d) to (f) $d = 2$ mm, $M = 70$ g and different aspect ratios a. Data are fitted by power laws (full lines).

for some experiments (Fig. 9cdef). This observed increase for high slope angles θ may be related to the change of dynamic regime of the granular flows when a saltating front appears at the flow front. The individual saltating particles could radiate higher seismic energy W_{el} at impact while barely contributing to the bulk potential energy and kinetic energy of the flow, causing the ratios $W_{el}/\Delta E_p$ and W_{el}/E_k to increase. We observe a slight decrease of the mean frequency f_{mean} as slope angle θ increases in some cases, but the variation is within the error bars (Fig. 9gh).



462 **Figure 9.** Seismic parameters as a function of the slope angle θ for the experiments on the
463 PMMA plate. (a),(b) Radiated seismic energy W_{el}. (c),(d) Ratio of W_{el} over the potential energy
464 lost ΔE_p. (e),(f) Ratio of W_{el} over the total kinetic energy E_k. (g),(h) Mean frequency f_{mean} of
465 the seismic signal for (a),(c),(e),(g) $d = 2$ mm, $a = 0.8$ and different masses M (different colors)
466 and (b),(d),(f),(h) $d = 2$ mm, $M = 70$ g and different aspect ratios a. Data of W_{el} in panels
467 (a) and (b) are fitted by the function $2.15 \cdot 10^{-3} H_0^2 (0.081/(\tan\delta - \tan\theta)^2 + 1)$, with H_0 the
468 column's initial height and $\delta = 27°$, the friction angle of the granular material (see section 4.1 for
469 explanations).

Table 3. Power laws $Y = bX^c$ used to fit the data in Fig. 10 and 11 and uncertainties Δb and Δc on parameters b and c. Coefficients are given in S.I. units.

Y	=	bX^c	Δb	Δc	R^2
A_{max}	=	$2.8 \cdot 10^{-4} \max(V_X^{COM})^{0.4}$	$\pm 8.5 \cdot 10^{-5}$	± 0.2	0.46
		$5.1 \cdot 10^{-4} \max(V_Z^{COM})^{0.55}$	$\pm 1.7 \cdot 10^{-4}$	± 0.086	0.77
		$4.2 \cdot 10^{-4} \max(V_{front})^{1.21}$	$\pm 5.5 \cdot 10^{-5}$	± 0.18	0.8
		$2.7 \cdot 10^{-4} \max(V_{summit})^{0.37}$	$\pm 2.5 \cdot 10^{-5}$	± 0.03	0.75
W_{el}	=	$10^{-4} E_k^{0.5}$	–	–	0.84
		$1.6 \cdot 10^{-4} E_k^{0.56}$	–	–	0.85
		$1.3 \cdot 10^4 d^3 M^{0.74} \max(V_{tot}^{COM})^{0.94}$	–	–	0.87
		$6 \cdot 10^3 d^3 M^{0.73} \max(V_{front})^{1.04}$	–	–	0.76

3.4 Relations Between Dynamics and Seismic Parameters

It is interesting to compare the maximum amplitude A_{max} and radiated seismic energy W_{el} of the seismic signal generated by a granular flow with the maximum flow speed of the front and of the center of mass in both X and Z-directions, in order to better understand which flow dynamic parameters has the most influence on the generated seismic signal, and thus could be extrapolated from the high-frequency seismic signal in the field (Fig. 10). The observed scaling laws are summed up in Table 3 (Normalized laws for W_{el} are given in Appendix C:).

Globally, the maximum seismic amplitude A_{max} matches better in time and amplitude with the maximum of the flow speed in the Z-direction than in the X-direction, as already reported by *Farin et al.* [2018] (Fig. 10a-d, see also section 3.2). We confirm these observations for various initial parameters M, a and d. Correlation between flow speed in the X-direction and seismic amplitude A_{max} is higher at high slope angles because the flow motion spends a longer duration in the X-direction than for small slope angles (Fig. 10ab). In the X-direction, there is no correlation between the maximum seismic amplitude A_{max} and the maximum speed of the center of mass at the horizontal, for $\theta = 0°$, because $V_X^{COM} = 0$ m s^{-1} while the seismic amplitude is not null. At high slope angles, A_{max} increases as $(\max(V_X^{COM}))^{0.5}$. A stronger correlation is observed between A_{max} and the maximum front speed $\max(V_{front})$ (at power ~ 1.2). In the Z-direction,

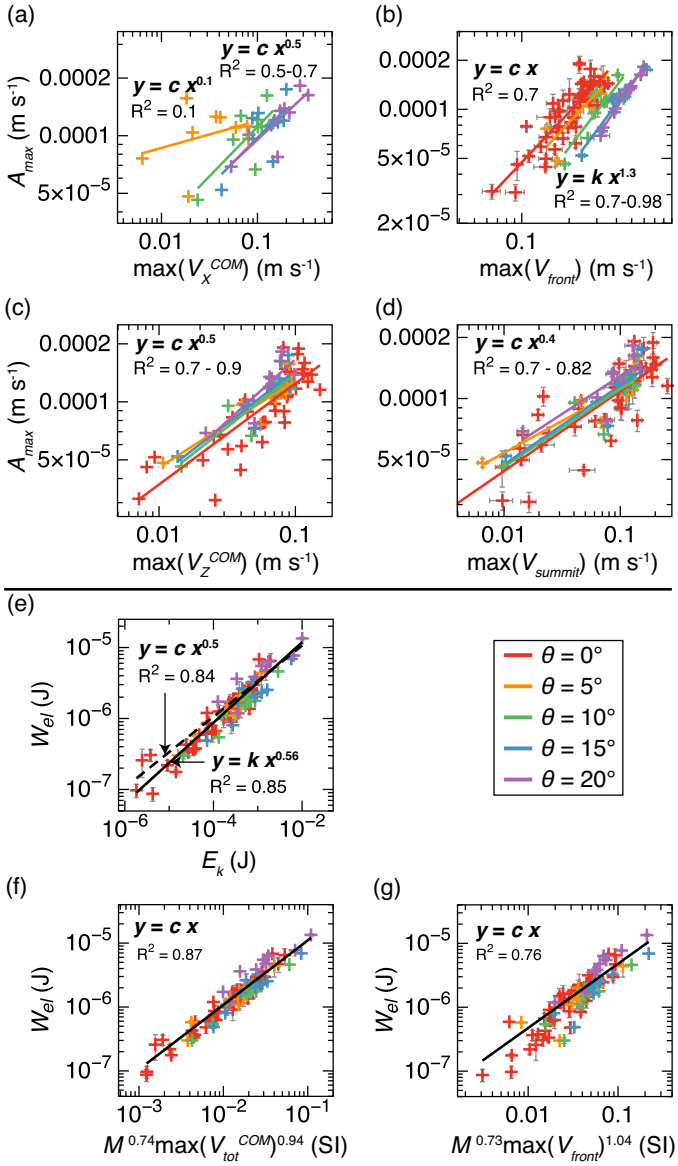


Figure 10. (a) to (d) Maximum amplitude A_{max} of the seismic envelope as a function of (a) the maximum speed $\max(V_X^{COM})$ of the center of mass in X-direction, (b) the maximum speed $\max(V_{front})$ of the flow front, (c) the maximum speed $\max(V_Z^{COM})$ of the center of mass in Z-direction and (d) the maximum speed $\max(V_{summit})$ of the summit. (e) Radiated seismic energy W_{el} as a function of the maximum kinetic energy E_k. (f) W_{el} as a function of the mass M and the maximum total speed of the center of mass $\max(V_{tot}^{COM})$. (g) Radiated seismic energy W_{el} as a function of M and the maximum speed of the flow front $\max(V_{front})$. The different colors are for different slope angles θ.

the maximum envelope amplitude A_{max} matches with the speed of the flow at power of $0.4-0.55$ for both V_Z^{COM} and V_{summit}, regardless of slope angle θ, with correlation coefficient $R^2 = 0.75 - 0.77$ (Fig. 10cd).

A more relevant speed to compare with the radiated seismic energy W_{el} seems to be the maximum total speed of the center of mass $\max(V_{tot}^{COM})$. Indeed, the radiated seismic energy W_{el} matches well with the square root of the maximum kinetic energy $E_k = \frac{1}{2} M \max(V_{tot}^{COM})^2$, with best fit observed as $E_k^{0.56}$ (Fig. 10e). W_{el} should then approximately increase as $M^{0.5} \max(V_{tot}^{COM})$. However, the best fit of W_{el} with adjustable power coefficients is $M^{0.74} \max(V_{tot}^{COM})^{0.94}$ independently of slope angle θ, with a good correlation coefficient $R^2 = 0.87$ (Fig. 10f). Thus, the radiated seismic energy W_{el} is almost proportional to the maximum total speed of the center of mass $\max(V_{tot}^{COM})$. The reason why W_{el} is not proportional to the column mass M as reported in Fig. 7e may be because $\max(V_{tot}^{COM})$ also slightly depends on M. We also observe a good correlation between the radiated seismic energy W_{el} and a function of the column's mass and the maximum front speed as $M^{0.73} \max(V_{front})^{1.04}$, although with a lower $R^2 = 0.76$ than for the relation with $\max(V_{tot}^{COM})$ (Fig. 10g). The fits of Fig. 10fg are for a given particle diameter $d = 2$ mm and we previously observed that $W_{el} \propto d^3$ (Fig. 7a). Consequently, for all of our experimental data, the radiated seismic energy W_{el} matches well with the following functions of the flow parameters (with $R^2 \approx 0.8$, Fig. 11ab)

$$W_{el} \approx 1.3 \cdot 10^4 d^3 M^{0.74} \max(V_{tot}^{COM})^{0.94}, \quad (8)$$

$$W_{el} \approx 6 \cdot 10^3 d^3 M^{0.73} \max(V_{front})^{1.04}. \quad (9)$$

Since these fits are independent of the column's initial aspect ratio a and slope angle θ, the previously observed dependence of the radiated seismic energy W_{el} to a and θ should then be included in the speeds $\max(V_{tot}^{COM})$ and $\max(V_{front})$. We discuss this below.

4 Discussion

4.1 Dependence on Slope Angle

We can interpret the increase of the radiated seismic energy W_{el} and of the maximum speeds $\max(V_{tot}^{COM})$ and $\max(V_{front})$ as a function of slope angle θ by comparing it with the increase of the flow runout distance r_f and flow duration t_f as θ increases. *Mangeney et al.* [2010] showed analytically that the runout distance r_f of granular flow

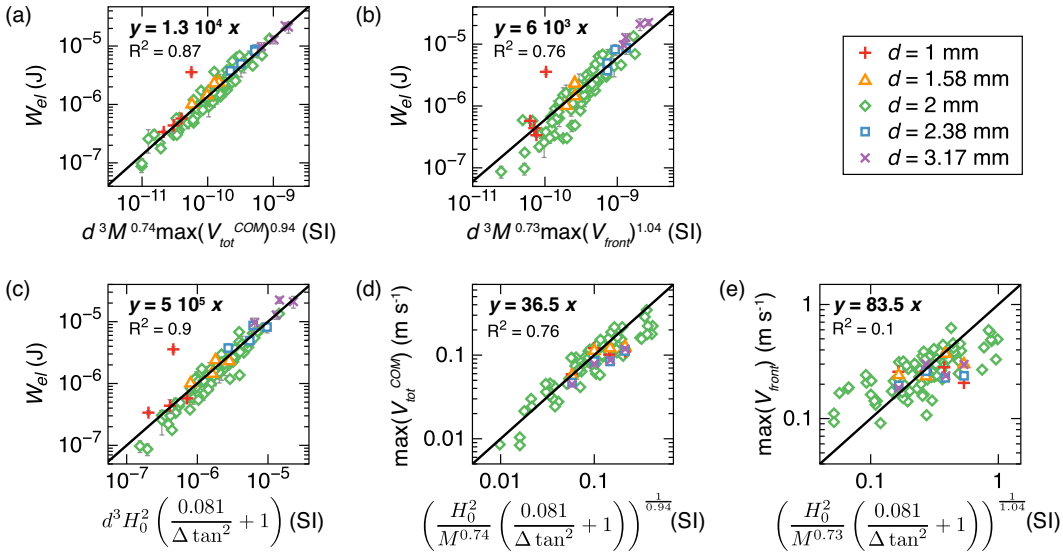


Figure 11. (a),(b),(c) W_{el} as a function of (a) $d^3 M^{0.74} \max(V_{tot}^{COM})^{0.94}$, (b) $d^3 M^{0.73} \max(V_{tot}^{COM})^{1.04}$ and (c) $d^3 H_0^2 (0.081/(\tan\delta - \tan\theta)^2 + 1)$, with M, the column mass, V_{tot}^{COM}, the total speed of the center of mass, V_{front}, the front speed, H_0, the initial column height, θ, the slope angle and δ, the friction angle, for different particle diameter d (different colored symbols). (d) Maximum total speed of the center of mass $\max(V_{tot}^{COM})$ and (e) Maximum speed of the flow front $\max(V_{front})$ as function of H_0, M and θ for different d. Data are compared with a scaling law $y = cx$, with c, a constant (full line).

Table 4. Parameters of the scaling laws $Y = c_1/(\tan\delta - \tan\theta)^b + c_2$ used to fit the data in Fig. 12, with δ, the friction angle and θ, the slope angle.

Y	=	$c_1/(\tan\delta - \tan\theta)^b + c_2$	R^2
r_f/H_0	=	$1.73/(\tan\delta - \tan\theta) - 1.58$	0.98
		$1.39/(\tan\delta - \tan\theta)$	0.93
t_s/τ_c	=	$3.85/(\tan\delta - \tan\theta) - 3.75$	0.95
		$3.02/(\tan\delta - \tan\theta)$	0.89
W_{el}/H_0^2	=	$1.72 \cdot 10^{-4}/(\tan\delta - \tan\theta)^2 + 2.15 \cdot 10^{-3}$	0.99

and its duration t_f are given by

$$r_f = \frac{2kH_0}{\tan\delta - \tan\theta}, \tag{10}$$

$$t_f = \frac{2\sqrt{k}\tau_c}{\tan\delta - \tan\theta}, \tag{11}$$

with H_0, the initial height of the granular column, δ, the friction angle of the granular material, k, a constant and $\tau_c = \sqrt{H_0/(g\cos\theta)}$, a characteristic time, with g the gravitational acceleration. r_f and t_f are inversely proportional to the parameter $\Delta\tan = \tan\delta - \tan\theta$ and thus diverge when the slope angle θ tends towards δ. The scaling law for the runout distance r_f has been validated experimentally by *Farin et al.* [2014] for granular flows of various volumes and aspect ratios inside an inclined flume, below a critical slope angle $\theta = 10° - 16°$. For slope angles θ above the critical angles the measured runout distances r_f were observed to diverge from the scaling law because they begin to also depend on the initial column length D_0.

In our experiments, the runout distance r_f and the flow duration t_f (or signal duration t_s, which is equal to t_f because of high signal-to-noise ratio) seem proportional to H_0 and τ_c, respectively, for a fixed slope angle θ (Fig. 12ab). In addition, r_f and t_s can be both well fitted by a law in $1/\Delta\tan$ for the whole investigated range of slope angles $\theta < 20°$, in agreement with Eq. (10) and (11) (dashed lines in Fig. 12ab, see also Table 4). The critical slope angle above which the runout distance r_f does not fit the analytical scaling law (10) any more seems to be higher than $\theta = 20°$. This is probably because the friction angle of our steel particles ($\delta = 27°$) is higher than the one in the experiments of *Farin et al.* [2014] ($\delta = 23°$).

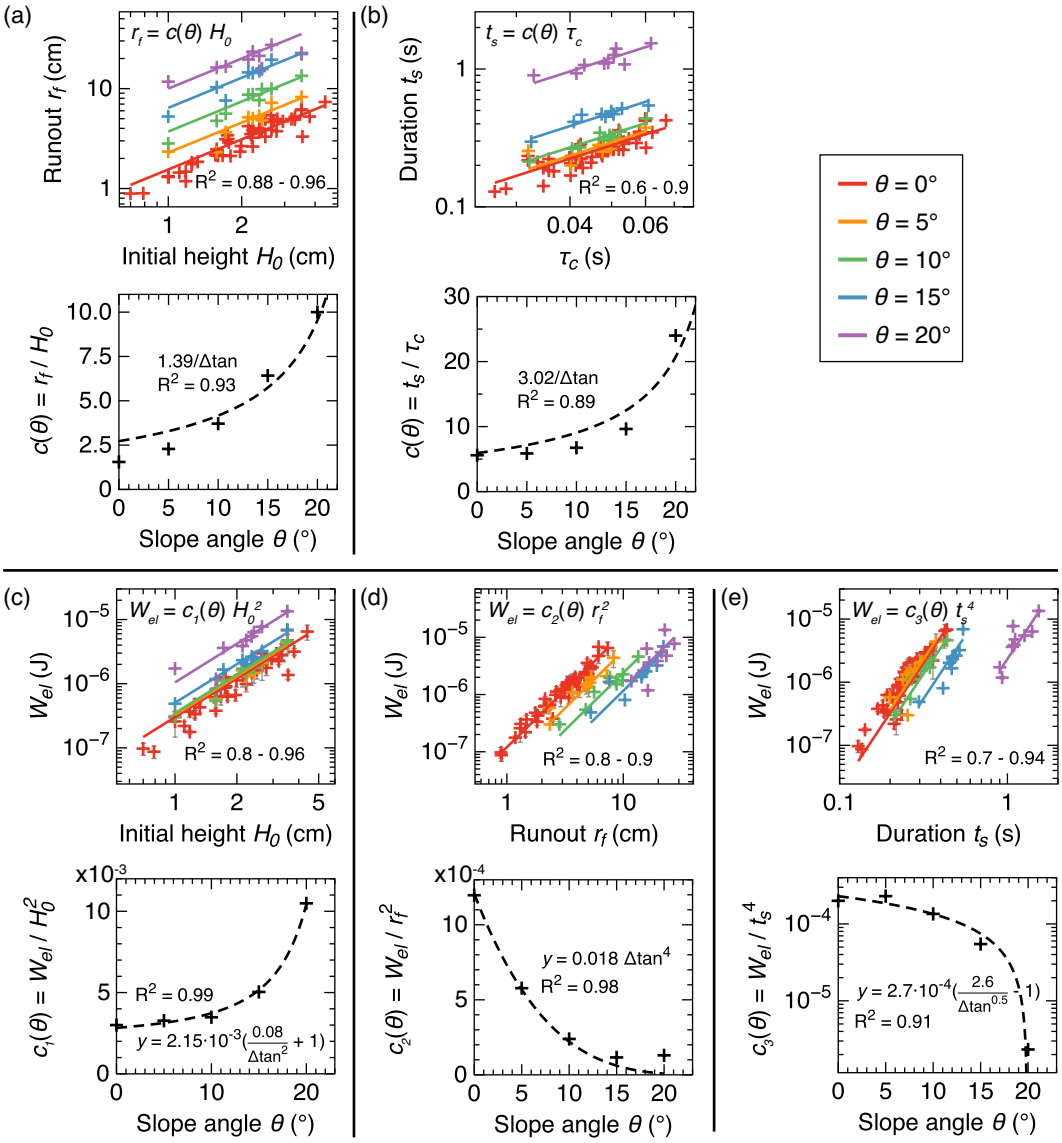


Figure 12. (a) Runout distance r_f as a function of the column initial height H_0. (b) Signal duration t_s as a function of characteristic time $\tau_c = \sqrt{H_0/(g\cos\theta)}$. (c) to (e) Radiated seismic energy W_{el} as a function of (c) initial height H_0, (d) runout distance r_f and (e) signal duration t_s, for different slope angles θ. In each panel, data for a given slope angle θ are fitted by a power law $y = c(\theta)x^n$, with n an integer and the coefficient $c(\theta)$ is represented as a function of the slope angle θ below each panel and fitted by a function of the parameter $\Delta\tan = \tan\delta - \tan\theta$ (dashed line).

Interestingly, for a fixed slope angle θ, the seismic energy W_{el} correlates well with the column's initial height H_0, the runout distance r_f and the flow/signal duration t_s as (Fig. 12cde)

$$W_{el} = c_1(\theta) H_0^2, \tag{12}$$

$$W_{el} = c_2(\theta) r_f^2, \tag{13}$$

$$W_{el} = c_3(\theta) t_s^4. \tag{14}$$

These laws are consistent with each others because $r_f^2 \propto H_0^2$ and $t_f^4 \propto H_0^2$ (Eq. (10) and (11)). The relation $W_{el} \propto t_s^4$ was predicted analytically by *Hibert et al.* [2011] for granular flows on a flat slope. Coefficients $c_i(\theta)$ in the scaling laws can be well fitted with a function of the parameter $\Delta \tan$ (Fig. 12cde). A good fit for $c_1(\theta)$ ($R^2 = 0.99$) is (in kg s^{-2})

$$c_1(\theta) \approx 2.15 \cdot 10^{-3} \left(\frac{0.081}{(\tan\delta - \tan\theta)^2} + 1 \right). \tag{15}$$

Using Eq. (12) and (15), we can very well fit the data of radiated seismic energy W_{el} as a function of θ for various mass M and aspect ratio a in Fig. 9ab, with no adjustments and using the real H_0 of each experiment and the friction angle $\delta = 27^\circ$ measured independently for steel beads of diameter $d = 2$ mm. The proportionality coefficient in equation (15) equals $2.15 \cdot 10^{-3}$ kg s^{-2} when $d = 2$ mm but depends on particle diameter as d^3. Thus, for all of our experimental data (Fig. 11c),

$$W_{el} \approx (5 \cdot 10^5 \text{kg m}^{-3}\text{s}^{-2}) \times d^3 H_0^2 \left(\frac{0.081}{(\tan\delta - \tan\theta)^2} + 1 \right). \tag{16}$$

A normalized law is given in Appendix C: . We can also express the radiated seismic energy W_{el} as a function of r_f or t_f and the slope angle θ, by replacing H_0 in Eq. (16) using Eq. (10) or (11), respectively.

From Eq. (8), (9) and (16), we finally deduce empirical expressions for the speeds $\max(V_{tot}^{COM})$ and $\max(V_{front})$ as a function of the other flow parameters (coefficients given in S.I. units, see Appendix C: for normalized laws)

$$\max(V_{tot}^{COM}) \approx 36.5 \left(\frac{H_0^2}{M^{0.74}} \left(\frac{0.081}{(\tan\delta - \tan\theta)^2} + 1 \right) \right)^{\frac{1}{0.94}} \tag{17}$$

$$\max(V_{front}) \approx 83.5 \left(\frac{H_0^2}{M^{0.73}} \left(\frac{0.081}{(\tan\delta - \tan\theta)^2} + 1 \right) \right)^{\frac{1}{1.04}} \tag{18}$$

Globally, our experimental data match well the scaling law for the maximum total bulk speed $\max(V_{tot}^{COM})$ ($R^2 = 0.76$) within an order of magnitude. However, the agreement

is less good for the maximum front speed $\max(V_{front})$ ($R^2 = 0.1$), probably because the position of the flow front is difficult to determine as the front is composed of saltating particles, especially at high slope angles (Fig. 11de).

4.2 Interpretation of the Empirical Scaling Laws with Particle Agitation

The amplitude of the seismic signal generated by granular flows is controlled by the rate of particle impacts R_{imp} at the bed and the impulse I_{imp} per particle impact on the bed. The rate of particle impact R_{imp} can be expressed as the number of impacts per particle per second per unit surface of the bed multiplied by the surface of the flow in contact with the bed. The impulse per particle I_{imp} is proportional to the mass of the particle multiplied by the particle impact speed. Individual particles in a granular flow have an average downslope speed and a fluctuating speed around their position [*Andreotti et al.*, 2013]. The fluctuating speed, that represents agitation of particles, is an important parameter that controls the rate at which particles impact each others and the bed but also controls the speed (i.e. the impulse) of the impacts on the bed. The fluctuating speed is then a key dynamics parameter to measure to better understand the seismic emission by granular flows[*Bachelet et al.*, 2017, 2018b]. Any change of the granular column initial dimensions or flow characteristics that increase the parameters R_{imp} and I_{imp} and the fluctuating speed thus also increase the radiated seismic energy W_{el}. The physical model for the seismic signal generated by debris flows proposed by *Farin et al.* [2019] shows that W_{el} scales in fact as $R_{imp}I_{imp}^2$ because the seismic amplitude generated by the sum of the impacts at the bed in the debris flow increases as $I_{imp}\sqrt{N}$, with N the number of impacts.

In order to quantify particle agitation, we measured the surface of the region of saltating particles in front of the flows (in the plane $(X, Y = 0, Z)$) (Fig. 13ab). Particle agitation is higher (i.e. the saltating surface is larger) as the slope angle θ, the flow mass M and the aspect ratio a increases. Saltation of particles at the flow front is quasi-absent at low slope angles $\theta < 10°$ [*Farin et al.*, 2018], but increases significantly at high slope angles $\theta > 15°$. Interestingly, we observe a linear correlation between the average fluctuating speed $\delta v = \sqrt{(v_X - \overline{v}_X)^2 + v_Z - \overline{v}_Z)^2}$ of flow particles, with v_i, the particle speed and $\overline{v}_i$, the average particle speed in i-direction (Fig. 13c). The best fit is $\delta v = 0.09{+}0.22\overline{v}_X$. We also note a linear correlation between the fluctuating speed δv of par-

ticles at the flow front and the speed V_{front} of the flow front at the time of the measurement (Fig. 13d). It is clear that a particle is more agitated when its speed or that of the whole flow increases because the flow is more unstable. Note however, that we measured the fluctuating speed of particles from the side of the flow and this speed may be lower than that at the middle of the flow. More laboratory experiments or numerical simulations are needed to link the radiated seismic energy W_{el} to the fluctuating speed δv of particles at the bed of granular flows and understand how δv is controlled by the other flow parameters (average flow speed in the case of steady granular flows, particle diameter, slope angle, column mass, flow thickness and bed roughness).

In light of these observations, we can interpret the dependence of W_{el} to the column or flow characteristics by determining which characteristics increase the rate of impacts R_{imp}, the impulse per impact I_{imp} and the particle fluctuating speed δv:

- When the flow speed or the slope angle θ increase, the rate of impacts per particle on the bed increases because particles are more agitated (δv increases) and encounter bumps on the bed faster. Note that, similarly to particle agitation, the radiated seismic energy W_{el} barely increases with slope angle θ for $\theta < 10^\circ$ but diverges as the slope angle θ approaches the friction angle δ (Fig. 9ab and 13ab). This confirms that the observed substantial increase of W_{el} at high slope angles θ may be linked to a change of granular flow regime towards an agitated flow.
- When the column mass M, the slope angle θ, the runout distance r_f or the flow duration t_s (which are both controlled by θ) increase, the surface of the flow in contact with the bed increases, therefore the number of particle impacts at the bed and W_{el} increase (Fig. 12de). The fact that W_{el} increases as r_f^2 is probably because the surface of the deposit in contact with the bed increases as r_f^2 (with the deposit width being proportional to the deposit length r_f).
- When the particle diameter d and the flow speed increase, particle impacts impart stronger impulses $I_{imp} \propto m v_{imp}$ on the bed. Indeed, the mass m of particles increases as d^3 and their impact speed v_{imp} increases as particle agitation δv increases, which itself increases with flow speed (Figure 13cd). In addition, when the initial column height H_0 or the aspect ratio a increase, the height of fall of the particles increase and they also impact the bed stronger.

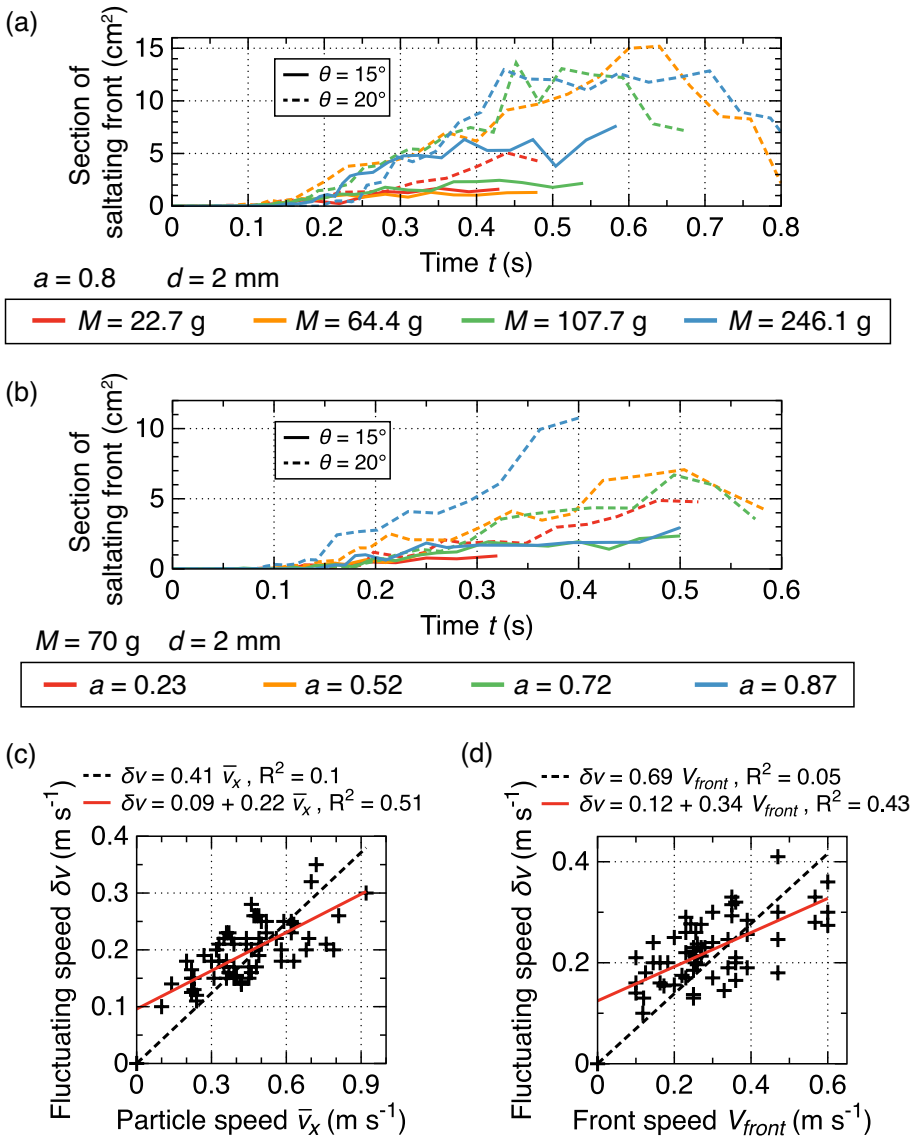


Figure 13. (a) and (b) Section of the saltating front as a function of time for $\theta = 15°$ (full lines) and $\theta = 20°$ (dashed lines) and for (a) $a = 0.8$, $d = 2$ mm and different masses M (different colors) and (b) $M = 70$ g, $d = 2$ mm and different column initial aspect ratios a (different colors). (c) Fluctuating speed $\delta v = \sqrt{(v_X - \overline{v}_X)^2 + (v_Z - \overline{v}_Z)^2}$ of particles measured from video recordings of various granular flows as a function of their average downslope speed $\overline{v}_x$ (in the $X direction$). (d) Fluctuating speed δv in the flow front as a function of the front speed V_{front} at the same time. In panels (c) and (d), linear (thick red line) and scale (black dashed line) fits of the data are shown with R^2 value.

4.3 Comparison with the Scaling Laws for a Single Particle Impact

Farin et al. [2015] demonstrated that for one single elastic impact of a particle on a smooth thin plate (without rough bed), the seismic energy radiated by the impact and the mean frequency of the generated seismic signal are related to the particle diameter d and normal impact speed v_Z as

$$W_{el} \propto d^5 v_Z^{11/5}, \tag{19}$$

$$f_{mean} \propto d^{-1} v_Z^{1/5}. \tag{20}$$

[*Bachelet et al.*, 2018a] verified that the scaling law for W_{el} is still valid when the particle impacts a rough bed made of particles glued on the thin plate. However, we observe in Fig. 7a that the empirical relation between the radiated seismic energy W_{el} and the particle diameter for a granular flow is different than that for a single particle impact because W_{el} clearly scales as d^3 and not as d^5. For a granular flow, the relation between W_{el} and d can be explained as follows. The rate of particle impact per particle and per unit surface R_{imp} varies as d^{-3} (because there are less particles per unit surface as d increases) and the squared impulse per particle impact I_{imp}^2 increases as d^6 because the impulse is proportional to the particle mass $m \propto d^3$. Therefore, if we refer to the physical model of *Farin et al.* [2019], then $W_{el} \propto R_{imp} I_{imp}^2 \propto d^3$, which is in agreement with our empirical observation.

For a granular flow, is not relevant to relate the radiated seismic energy W_{el} and the normal impact speed v_Z of the individual particles as we do for one single impact because each particle of the flow has a different speed at a given time. As discussed earlier, a more relevant particle speed to relate to W_{el} in granular flows is the fluctuating speed δv of the particles, in conjunction with the rate of particle impact (which has no meaning for a single impact).

We note that the mean frequency f_{mean} of the seismic signal generated by granular flows decrease as as particle diameter d increases, in agreement with what is observed for a single impact (Fig. 7d). However, f_{mean} seems to depend less on d (at power -0.15) than for a single impact (power -1). The exact scaling law between f_{mean} and d is unsure due to the large uncertainties on the frequency. The range of investigated particle diameters d may not be large enough to clearly determine the relation between f_{mean} and d. Moreover, the low dependence of f_{mean} on d in our experiments may be explained

by the fact that high frequencies are filtered out by the presence of the rough bed on the plate, which was not present in the study of *Farin et al.* [2015].

4.4 Comparison with the Field

4.4.1 Seismic efficiency

Some field studies estimated the ratio of radiated seismic energy over the potential energy lost by the gravitational event $W_{el}/\Delta E_p$ (i.e. the seismic efficiency). From site to site, $W_{el}/\Delta E_p$ varies over several orders of magnitude, from 10^{-6} to 0.25 [*Vilajosana et al.*, 2008; *Deparis et al.*, 2008; *Hibert et al.*, 2011; *Lévy et al.*, 2015; *Farin et al.*, 2015; *Hibert et al.*, 2017c]. The discrepancy of $W_{el}/\Delta E_p$ observed in the field could potentially be explained by a variation of the average, or characteristic, particle diameter d or (less probably) a variation of the slope angle θ. Indeed, in our experiments, $W_{el}/\Delta E_p$ and W_{el}/E_k strongly increase with particle diameter as d^3 and also slightly depend on the slope angle θ (Fig. 7bc and 9cdef). That said, the presence of a rough or erodible bed on bedrock also strongly affects the seismic efficiency of granular flows in the field, as discussed by *Bachelet et al.* [2018a] and *Farin et al.* [2018], but this effect is complex and still not well understood. Moreover, contrary to laboratory experiments where impacts are mostly elastic, impacts of natural rock blocks in the field are often plastic because the blocks can fracture themselves or the bed and break into pieces during impacts. Consequently, energy ratios $W_{el}/\Delta E_p$ and W_{el}/E_k strongly depend on the mineralogical composition of the impactors and the ground which can be very different from one site to the other, thus causing further discrepancy. The energy budget of inelastic impacts has been discussed in details by *Farin et al.* [2015].

4.4.2 Relation between Radiated Seismic Energy and Flow Volume

Norris [1994] and *Yamada et al.* [2012] observed that the maximum amplitude $A_{max} \propto W_{el}^{0.5}$ of the seismic signal generated by large landslides ($V = 10^4$–10^7 m^3) scales with their volume V. In contrast, *Hibert et al.* [2011] reported a linear correlation between the seismic energy radiated by rockfalls and their volume V ($V = 10 - 10^4$ m^3). In our experiments, the radiated seismic energy W_{el} scales as the flow mass M (which is proportional to the flow volume V, for a given particle diameter d). Our results are then in agreement with the observations of *Hibert et al.* [2011] but not with that of *Norris* [1994]

and *Yamada et al.* [2012], for which $W_{el} \propto M^2$. The discrepancy between the different studies may originate from different relative sizes of the events compared to the particle size. Indeed, our experiments compare more with small rockfalls as those observed by *Hibert et al.* [2011] than to large landslides (which may also contains water) as that observed by *Norris* [1994] and *Yamada et al.* [2012]. Furthermore, the frequency range over which the radiated seismic energy W_{el} is measured may also affect the observed scaling law between W_{el} and M. Indeed, in the case of *Norris* [1994] and *Yamada et al.* [2012] studies, the distance between the source and the seismic stations is in general several tens of kilometers while the rockfalls recorded by *Hibert et al.* [2011] occur for 50 m to 2 km away from the seismic stations. Frequencies of the seismic signal are lower as the source/station distance increases. The scaling $W_{el} \propto M$ reported by *Hibert et al.* [2011] and in the present study may be more representative of high-frequency (> 1 Hz) processes that occur at the particle scale than the relation $W_{el} \propto M^2$ found by *Norris* [1994] and *Yamada et al.* [2012] that may be more representative of low-frequency (< 1 Hz), large scale processes (e.g. bulk motion). The state of damage of the ground over which the granular flow propagate and the presence of an erodible bed may also affect the relation between W_{el} and M, as it has been noted for single particle impacts [*Bachelet et al.*, 2018a]. The relation between W_{el} and M may also depend on the thickness of the impacted substrate. For example, *Farin et al.* [2015] demonstrated that the scaling laws between the mass and speed of an impacting particle and the characteristics of the generated seismic signal were different on a thin plate or thick block. We conducted some granular column collapse experiments on a thick marble block of dimensions $20 \times 20 \times 20$ cm^3 (see Fig. A.1 in Appendix B:). On the thick block, the radiated seismic energy W_{el} increases as $M^{1.5}$ and energy ratio $W_{el}/\Delta E_p$ is independent of M (Fig. A.1ab), in contrast to what is observed on the thin plate ($W_{el} \propto M^{1.0}$ and $W_{el}/\Delta E_p \propto M^{-0.3}$, Fig. 7ef). More experiments of granular flows on thick blocks are needed to better understand the effect of the thickness of the substrate on the empirical scaling laws and extrapolate them to the field.

4.4.3 Relation between Radiated Seismic Energy and Flow Momentum

For twelve large landslides that occurred worldwide between 1994 and 2014, *Hibert et al.* [2017a] reported that the amplitude of the seismic signal envelope filtered between 3 and 10 Hz matches well temporally with the variation of the flow bulk momen-

tum in the downslope direction, inferred from the low-frequency content (< 0.1 Hz) of the seismic signal. In addition, they found that the maximum envelope amplitude increases linearly with the flow momentum MV_X^{COM}. Therefore, in their case $W_{el} \propto (M \max(V_X^{COM}))^2$. In our experiments, the shape of the seismic envelope does not match with the speed of the center of mass in X-direction and the maximum envelope amplitude matches better with the maximum of the speed of the center of mass in the Z-direction (Fig. 5ag and 10ac) [see also *Farin et al.*, 2018, for more details]. The best fit we observe is $W_{el} \propto M^{0.74} \max(V_{tot}^{COM})^{0.94}$ (Fig. 10f), which is different by about a power of 2 from *Hibert et al.* [2017a] scaling law.

The first explanation of this difference may be that the flows considered by *Hibert et al.* [2017a] spend a longer proportion of their total duration with a motion in the X-direction, with motion in the Z being almost null for most of the flow propagation. Thus $V_{tot}^{COM} \approx V_X^{COM}$ in their case and the radiated seismic amplitude can only match with flow motion in the X-direction. In contrast, in our experiments, flow motion in both X and Z-directions contributes to the seismic generation and, in consequence, the radiated seismic energy correlates well with the total speed of the center of mass (Fig. 11a). The second explanation of the difference with the observations of *Hibert et al.* [2017a] is the same as the one we invoked to explain why we observe $W_{el} \propto M$ instead of $W_{el} \propto M^2$ as observed by *Norris* [1994] and *Yamada et al.* [2012]. In *Hibert et al.* [2017a] study, the good correlation between the seismic envelope amplitude and the flow bulk momentum in X-direction may more originate from bulk related processes (bulk motion, long-scale topographic variations), while in our experiments seismic amplitude may more be related to particle scale processes (particle diameter, speed fluctuations,...). Indeed, the seismic signals of *Hibert et al.* [2017a] are recorded far from the flows and seismic signals are in a relatively low frequency range (3-10 Hz) while particle impacts in the field can generate signals of frequency up to 150 Hz [e.g. *Helmstetter and Garambois*, 2010; *Hibert et al.*, 2011; *Dammeier et al.*, 2011; *Farin et al.*, 2015; *Hibert et al.*, 2017c].

4.4.4 Scaling Laws Between Flow Dynamic Parameters

Aside from seismic waves generation by granular flows, we now discuss two empirical scaling laws reported in the literature between dynamic parameters of granular flows, in light of our laboratory experiments.

Ekström and Stark [2013] reported the relation $M \approx (0.54\ \mathrm{m^{-1}s^2})F_{max}$ between the mass M of 29 large landslides and the maximum force $F_{max} = M \max|A_X^{COM}|$ they applied on the ground. The maximum force F_{max} is deduced by inversion of the low-frequency seismic signals. Our experimental data also match this relation $M \approx 0.54M \max|A_X^{COM}|$, within an order of magnitude (Fig. 14a). However, we observe that the peak bulk acceleration $\max|A_X^{COM}|$ is approximately independent of the flow parameters and is about $2\pm1\ \mathrm{m\ s^{-2}}$ (Fig. 14b). Similarly, the peak bulk acceleration evaluated by *Ekström and Stark* [2013] is about $2\pm1\ \mathrm{m\ s^{-2}}$ for all landslides. As a consequence, the relationship $M \approx 0.54M \max|A_X^{COM}|$ may be artificially caused by the fact that we are plotting the mass M as a function of itself times a constant which is $(0.54\ \mathrm{m^{-1}s^2}) \max|A_X^{COM}| \approx 1$.

For different large landslides that occurred in Japan and the ones reported by *Ekström and Stark* [2013], *Yamada et al.* [2018] found a scaling law $\max(V_X^{COM}) \approx 2(\Delta H^{COM})^{0.5}$, relating $\max(V_X^{COM})$, the maximum speed of the center of mass in the X-direction and ΔH^{COM}, the height difference of the center of mass before and after the collapse. We observe a similar scaling law in our experiments for $d = 2$ mm and different masses M and aspect ratios a, with a power about 0.53 when we fit all of our data for all slope angles θ (Fig. 14c). However, for a given slope angle θ, the maximum bulk speed seems to increase as $\max(V_X^{COM}) \approx 2(\Delta H^{COM})^{1.2}$. Therefore, the relation reported by *Yamada et al.* [2018] may be due to the fact that the different landslides occurred at different slope angles θ. This illustrates an advantage of the laboratory experiments of granular flows as the ones conducted in the present study: we can separate the different controlling parameters and better understand the link between different flow characteristics.

4.5 What Flow Parameters Could Be Inverted from High-Frequency Seismic Signals in the Field?

The preceding sections showed that there are some differences between the scaling laws reported in the field between dynamics and seismic characteristics of granular flows and that observed in the laboratory. Even if an empirical scaling law represents very well the laboratory data, for example $W_{el} \approx 1.3{\cdot}10^4 d^3 M^{0.74} max(V_{tot}^{COM})^{0.94}$ (Fig. 11a), it is unclear that the exact same scaling law will match the field data because processes are still not well understood, such as the effect of the complex bed topography on the high-frequency seismic signal, how seismic energy is attenuated in a erodible bed or

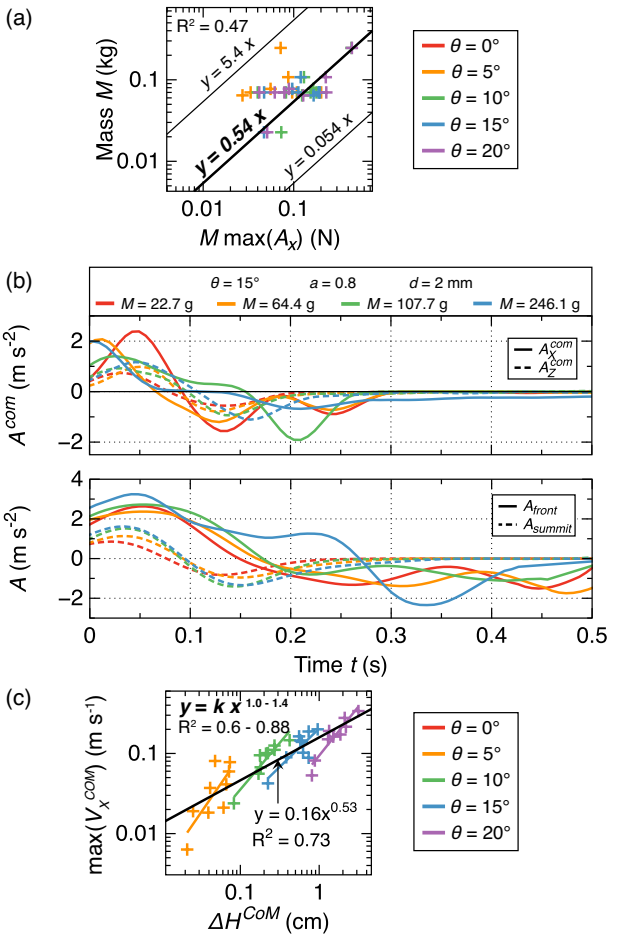


Figure 14. (a) Mass M of the granular columns as a function of $M\max(A_X)$, with A_X, the acceleration of the flow center-of-mass in the X-direction, for different slope angles (different colors). (b) Acceleration of the center of mass in both X and Z-directions and acceleration of the flow front and summit for $\theta = 15°$, $a = 0.8$, $d = 2$ mm and different column's mass M. (c) Maximum speed $\max(V_X^{COM})$ of the center of mass in the X-direction as a function of the height difference ΔH^{COM} of the center of mass before and after the collapse, for different slope angles θ (different colors).

particle segregation. Nevertheless, the empirical scaling laws established in the laboratory allow us to observe which flow properties have the strongest influence on a given seismic characteristic and, therefore, may be inferred from this characteristic in the field. Note that, however, if one wants to evaluate any flow properties quantitatively from the seismic signal, we have to have a good estimate of the ground elastic parameters (density, quality factor and wave speeds), because these are necessary to compute the absolute radiated seismic energy W_{el} [e.g. *Vilajosana et al.*, 2008; *Hibert et al.*, 2011; *Lévy et al.*, 2015; *Hibert et al.*, 2017c]. Without these elastic parameters, we can only make qualitative estimates of flow characteristics between successive granular flows [e.g. *Kean et al.*, 2015].

4.5.1 Particle diameter

The radiated seismic energy W_{el} and the seismic efficiency ($W_{el}/\Delta E_p$ or W_{el}/E_k) strongly depend on particle diameter as d^3 (Fig. 7abc). The characteristic particle diameter d of the granular flow could thus be inverted from these parameters, provided the other flow parameters also affecting these parameters (mass M, flow speed, aspect ratio a) are known. The average frequency f_{mean} of the seismic signal generated by the granular flows seem to only depend on the particle diameter d (Fig. 7d), then it could be a useful parameter to obtain information on the characteristic particle diameter of the granular flow. The relevant characteristic particle diameter contributing most to the seismic signal amplitude depends on the particle size distribution. *Farin et al.* [2019] evaluated that this characteristic diameter corresponds to the 73th percentile of the particle size distribution (d_{73}) for a debris flow with a log-'raised cosine' particle size probability distribution. Note that if one would like to evaluate another flow parameter, the characteristic particle diameter could also be determined from sampling of the deposits of prior granular flows at the investigated site.

4.5.2 Mass

The only seismic parameters that seem to have a strong dependence on the flow mass M is the radiated seismic energy W_{el} (Fig. 7e). Using relations as the ones in Eq. (8) or (9), one could invert the flow mass M from W_{el} if the characteristic particle diameter d and the flow speed are known.

4.5.3 Aspect Ratio

The radiated seismic energy W_{el} and the seismic to kinetic energy ratio W_{el}/E_k clearly depend on the column initial aspect ratio a (Fig. 7ik) and could thus potentially give some quantitative information about this parameter if the particle diameter d can be independently estimated.

4.5.4 Flow Speed

The average or frontal speed of the granular flows relate well with the radiated seismic energy (Fig. 11ab). The flow speed could then be extrapolated from W_{el} if the characteristic particle diameter d and the flow mass M are known. It is possible that, for natural granular flows, the correlation between the radiated seismic energy and the speed of the flow front is better than in our experiments because large particle diameters often accumulate at the front of the flow due to particle segregation [*Iverson*, 1997].

If one wants to determine another flow parameter (flow mass M or particle diameter d) from the radiated seismic energy W_{el}, the average flow speed could also be determined from optical methods (cameras, laser distancemeters,...) or other seismic methods. For example, the trajectory of the flow center-of-mass and thus the average flow speed could be deduced from low-frequency (< 0.1 Hz) signals for large landslides [*Allstadt*, 2013; *Hibert et al.*, 2014a]. Moreover, if two seismic stations are located a few meters away along the flow path, the cross-correlation of the seismic signals measured could constrain the time spent by the flow to travel from one station to the other and therefore the average flow speed between the two stations [*Arattano and Marchi*, 2005; *Burtin et al.*, 2010; *Kean et al.*, 2015].

4.5.5 Runout Distance and Flow Duration

We observed a good correlation between the squared runout distance r_f^2 and the radiated seismic energy W_{el} for a given slope angle θ (Fig. 12d). If the slope angle of a specific site is known, one could potentially automatically evaluate the runout distance of landslides occurring at a site from their radiated seismic energy. More work is however required to verify if the relation $W_{el} \propto r_f^2$ observed here for a constant flat slope changes for a curved slope as one encounter in nature or for a different bed roughness. Numerical simulations of granular flows coupled with a model of seismic generation by

impacts could also provide insights into the influence of complex bed topography on the relation between r_f and W_{el}. The duration of the flow approximates well with the duration of the seismic signal as long as the signal-to-noise ratio is high.

4.5.6 Inversion Test

We attempt to invert the particle diameter d, aspect ratio a and mass M of all of our released granular columns released from the characteristics of the generated seismic signal using the obtained empirical scaling laws. By inversion of the scaling laws in Tables 2 and 3, we get (with coefficients in S.I. units, see Appendix C: for normalized laws)

$$d \approx 2.77 \cdot 10^{22} (f_{mean})^{-6.66} \quad (21)$$

$$a \approx 0.014 \left(\frac{W_{el}}{E_k} \right)^{-0.77} \quad (22)$$

$$M \approx 6.67 \cdot 10^{-6} \left(\frac{W_{el}}{d^3 \max(V_{front})^{1.04}} \right)^{1.37} \quad (23)$$

$$M \approx 2.76 \cdot 10^{-6} \left(\frac{W_{el}}{d^3 \max(V_{tot}^{COM})^{0.94}} \right)^{1.35} . \quad (24)$$

Using these equations and if we assume that the flow speeds V_{front} and V_{tot}^{COM} (and thus kinetic energy E_k) can be measured e.g. using a camera or from low frequencies, one can retrieve d, a and M from a measurement of the mean frequency f_{mean} and the seismic energy W_{el} of the generated high-frequency seismic signal (Fig. 15). Most of the inverted particle diameters d and aspect ratios a using Eq. (21) and (22), respectively, are close to their real values, within a factor of two (Fig. 15ab). Using the diameters d inverted in Fig. 15a, one can also retrieve the flow mass M from the radiated seismic energy and the flow speeds using Eq. (23) and (24), but within more than an order of magnitude (Fig. 15ce). Estimating the particle diameter d from the signal frequency f_{mean} is somewhat imprecise because f_{mean} only has a small dependence to d at power -0.15 (Table 2). If particle diameter is evaluated using another method described above, a much better estimation of the flow mass is obtained using the real particle diameters d, within a factor of 2 for most cases (Fig. 15df). A better agreement between inverted and real masses M is obtained using the speed of the center of mass V_{tot}^{COM} than when using the flow front speed V_{front}. Note that we doubt that the inverted scaling laws (21) to (24) could be directly applied to estimate the parameters of natural granular flows from the generated seismic signal because they are obtained in a simple, somewhat unrealistic,

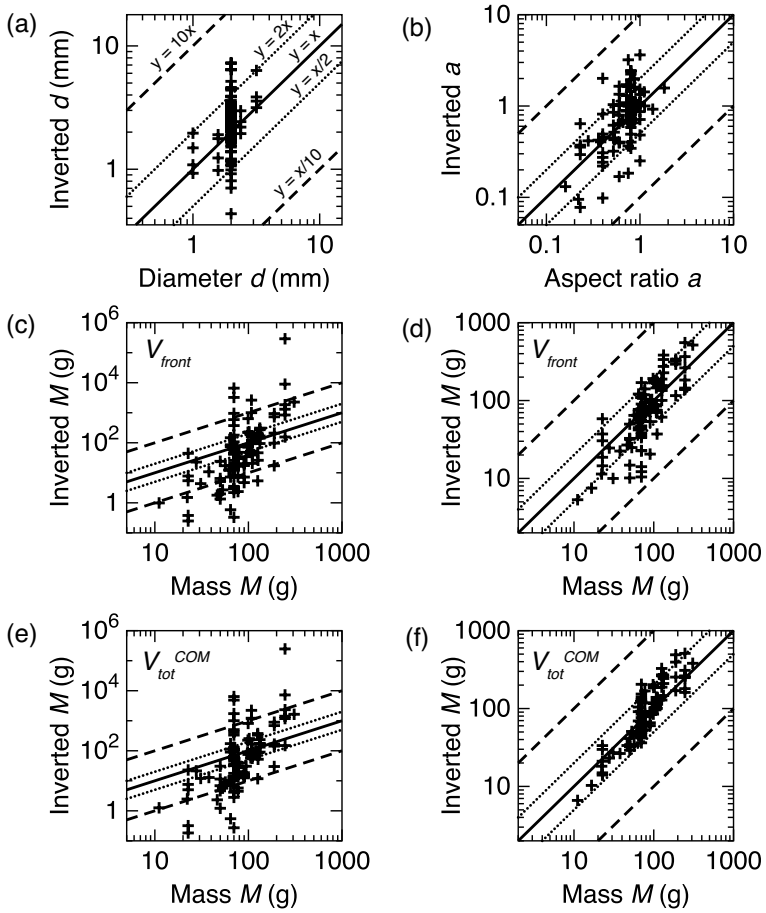


Figure 15. Inversion of the parameters of all of the granular flows from seismic characteristics and the flow speeds using equations (21) to (24). (a) Particle diameter inverted from the mean frequency of the seismic signal f_{mean}. (b) Aspect ratio a inverted from the ratio W_{el}/E_k. (c) to (f) Mass M inverted from the radiated seismic energy W_{el}, diameter d with (c), (d) the speed of the flow front V_{front}, (e), (f) the total speed of the flow center of mass V_{tot}^{COM} and using (c), (e) the particle diameter inverted in (a) and (d), (f) the exact particle diameter d. Dashed lines are $y = 10x$ and $y = x/10$ laws, dotted lines are $y = 2x$ and $y = x/2$ laws and the full line is $y = x$.

configuration. However, they give insights into which seismic parameters have the strongest influence on a given flow characteristic.

5 Conclusions

We conducted laboratory experiments of 3D granular column collapse on an inclined flat thin plate. We successively varied the column mass and aspect ratio, the particle di-

ameter and the slope angle. The dynamic parameters of the granular flows were recorded using a fast camera and the generated seismic signal was measured using piezoelectric accelerometers. The conclusions of these experiments are as follows:

1. The observations of *Farin et al.* [2018] for one column mass, aspect ratio and particle diameter remain valid when these parameters change. Specifically, the maximum seismic amplitude coincides in time with the maximum flow speed in the direction normal to the bed. The seismic amplitude starts to depend on the flow motion in the downslope direction during the deceleration phase when flow motion in normal direction has stopped. The shape of the temporal variation of the normalized radiated seismic energy and potential energy lost by the granular flow match and this shape changes when the slope angle is higher than a critical slope angle $\sim 15°$.
2. Empirical scaling laws are established for the seismic characteristics as a function of the parameters of the granular column and of the deposit. The absolute radiated seismic energy scales with particle diameter as d^3, column mass as M, aspect ratio as $a^{1.1}$ and initial column height as H_0^2 when all other parameters are fixed. We also observe that the radiated seismic energy scales with the squared runout distance and with flow duration at power 4. The ratio of seismic energy over potential energy lost is between $3 \cdot 10^{-5}$ and $2 \cdot 10^{-3}$ and mostly increases with particle diameter as d^3. The ratio of seismic energy over bulk kinetic energy is between $7 \cdot 10^{-4}$ and 10^{-1} increases as d^3 and decreases as $a^{-1.3}$. The average frequency of the radiated seismic signal only depends on the particle diameter as $d^{-0.15}$. The powers of these scaling laws do not strongly depend on slope angle.
3. Very good correlation is found for all of our experiments ($R^2 = 0.87 - 0.9$) between the seismic energy radiated by the granular flows and two equivalent functions of the flow characteristics $d^3 M^{0.74} \max(V_{tot}^{COM})^{0.94}$ and $d^3 H_0^2 \left(\frac{0.081}{(\tan\delta - \tan\theta)^2} + 1 \right)$, with d, the particle diameter, M, the flow mass, V_{tot}^{COM}, the total speed of the flow center-of-mass, H_0, the column initial height, δ, the friction angle and θ, the slope angle. The observed scaling laws allow us to determine which flow parameters could be inferred from a given seismic characteristic in the field. For example, particle diameter, flow mass or flow average speed can be deduced from the radiated seismic energy if the other two parameters can be determined independently. By assuming the flow average speed is known, we show that we can retrieve parame-

ters d, a and M from the seismic signal within a factor of two. These scaling laws provide insights into what relations can be tested in the field between flow and seismic parameters.

4. We interpreted the scaling laws for the radiated seismic energy by discussing particle agitation in the flows. For example, the radiated seismic energy is almost constant at small slope angle but significantly increases after a critical slope angle. This increase correlates with a similar increase of particle agitation (fluctuating speed) and, therefore, is probably caused by a change of the dynamic regime of granular flows towards a more agitated flow. Moreover, the seismic efficiency decreases as slope angle increases but increases again at high slope angles, probably because the stronger particle agitation increases the radiated seismic energy while not contributing much to bulk potential energy. More generally, any change in the flow parameters that increases the particle fluctuating speed at the bed, which controls the rate of particle impact and the force per impact on the bed, also increases the radiated seismic energy. Fluctuating speed is therefore a crucial parameter to measure in future laboratory experiments in order to better understand the link between flow parameters and the generated high-frequency (> 1 Hz) seismic signal.

The present laboratory experiments provide an extensive set of data to test future numerical simulations of the high-frequency seismic signal generated by granular flows. Such simulations would be useful to better understand the quantitative link between the fluctuating speed of particles (i.e. particle agitation) and the seismic energy radiated by granular flows and the role of the complex bed topography on the shape of the seismic signal. More seismically monitored experiments are also needed on an erodible bed because the structure of the flow/bed interface is thought to have a critical influence on the high-frequency seismic efficiency of granular flows. Understanding these complex processes (particle fluctuations in flows, effect of bed topography, erodible bed) is crucial to be able to infer quantitative flow characteristics from seismic signals in the field in the future, even if very clear empirical scaling laws can be established at the laboratory scale.

A: Granular Column Collapse Experiments on a Thick Block

In order to verify how the scaling laws depend on the thickness of the substrate, we conducted a series of granular column collapse experiments on a marble block of dimensions $20 \times 20 \times 20$ cm^3 for various column masses 10 g $< M <$ 200 g and aspect ratios $0.2 < a < 2.0$. The radiated seismic energy W_{el}, the ratio of W_{el} over the potential energy lost ΔE_p and the mean frequency f_{mean} measured in these experiments are shown in Fig. A.1. Similar scaling laws to the thin plate case are observed for the aspect ratio a (Fig. A.1def). The mean frequency f_{mean} seems to very slightly increase with M and a (Fig. A.1cf). Refer to section 4.4.2 for discussion of the data as a function of the column's mass M.

B: Seismic Signals and Comparison with Dynamics for Different Aspect Ratios

In this Appendix, we show seismic signals and spectrograms for different aspect ratios and fixed mass $M = 110$ g and particle diameter $d = 2$ mm, for slope angles $\theta = 0^\circ$ and $\theta = 15^\circ$ (Fig. B.1 and B.2). The comparison of the seismic signals with the dynamic characteristics of the granular flows for different aspect ratios at $\theta = 0^\circ$ and $\theta = 15^\circ$ and for different masses at $\theta = 0^\circ$ is shown in Fig. B.3, B.4 and B.5. Refer to section 3 for discussion of these Figures.

C: Normalized Scaling Laws

In this section, we give a normalization of the scaling laws obtained in the manuscript. We normalize the parameters by those for one single impact of a steel particle of diameter $d_{part} = 1$ mm, mass $M_{part} = 4 \cdot 10^{-6}$ kg, impact speed $V_{part} = \sqrt{gd} \approx 0.1$ m s^{-1} and fall height $H_{part} = d/2$. Therefore, the normalized parameters are $d' = d/d_{part}$, $M' = M/M_{part}$, $\max(V_{tot}^{COM})' = \max(V_{tot}^{COM})/V_{part}$, $\max(V_{front})' = \max(V_{front})/V_{part}$ and $H_0' = H_0/H_{part}$. The radiated seismic energy W_{el} is normalized by the theoretical radiated seismic energy for the impact of a steel particle with the above characteristics on the PMMA plate, $W_{part} \approx 8.85 \cdot 10^{-11}$ J [*Farin et al.*, 2015]. The kinetic energy is normalized by the kinetic energy of the impact $E_{part} = \frac{1}{2} M_{part} V_{part}^2 \simeq 2 \cdot 10^{-8}$ J. Then, the normalized energies are $W_{el}' = W_{el}/W_{part}$ and $E_k' = E_k/E_{part}$. The frequency is normalized by 1 Hz.

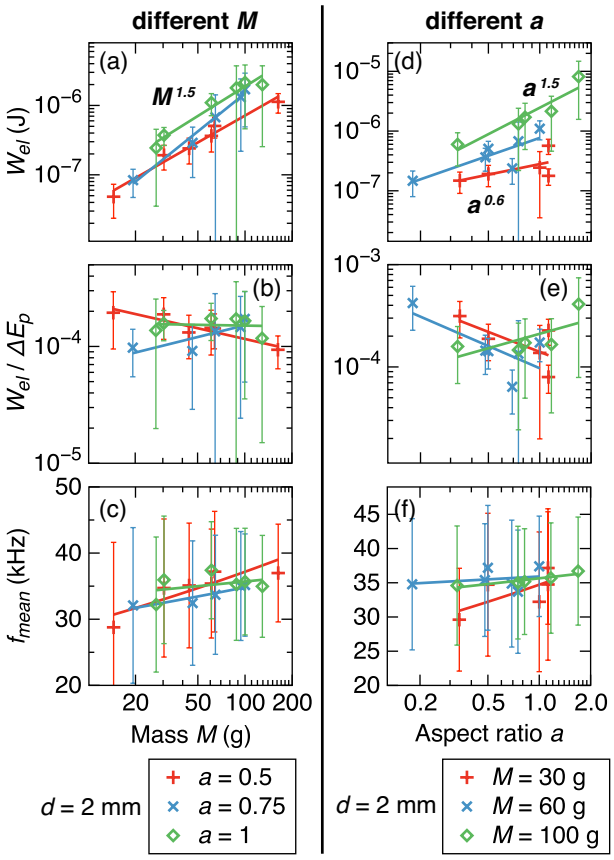


Figure A.1. Seismic parameters as a function of the granular column parameters for the experiments on a marble block of dimensions 20 × 20 × 20 cm^3. (a),(d) Radiated seismic energy W_{el}, (b),(e) Ratio of W_{el} over the potential energy lost ΔE_p, (c),(f) Mean frequency f_{mean} of the seismic signal for (a) to (c) different masses M for d = 2 mm and fixed aspect ratios a and (d) to (f) different aspect ratios a for d = 2 mm and fixed masses M. Data are fitted by power laws (full lines). The power law is indicated when a tendency is observed.

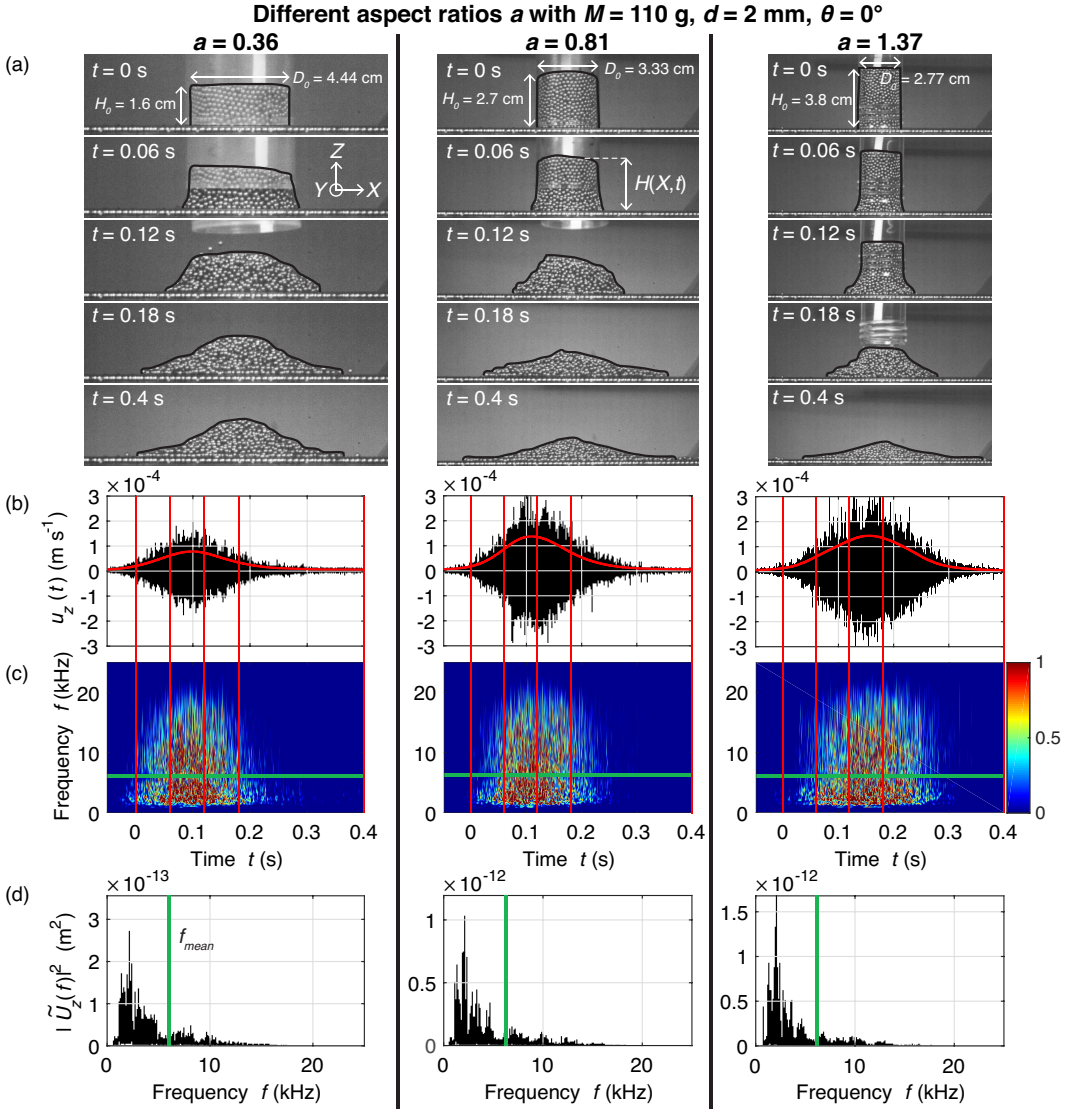


Figure B.1. (a) Successive pictures of three horizontal ($\theta = 0°$) granular column collapse experiments with different aspect ratios $a = 0.36$, $a = 0.81$ and $a = 1.37$, all with initial column mass $M = 110$ g and particle diameter $d = 2$ mm. The black lines show the contours $H(X,t)$ of the granular flows that are used to compute the flow dynamic parameters. (b) Seismic signals (i.e. plate vibration speed $u_Z(t)$) generated by the granular flows as a function of time t. The red line represent the amplitude envelope, filtered below 5 Hz. (c) Spectrograms of the signals. Warmer colors mean more energy (normalized to 1). (d) Squared amplitude spectra $|\tilde{U}_Z(f)|^2$ of the seismic signals. The vertical red lines in panels (b) and (c) indicate the times of the pictures in (a) and the thick green line in panels (c) and (d) indicates the mean frequency f_{mean} of the signals.

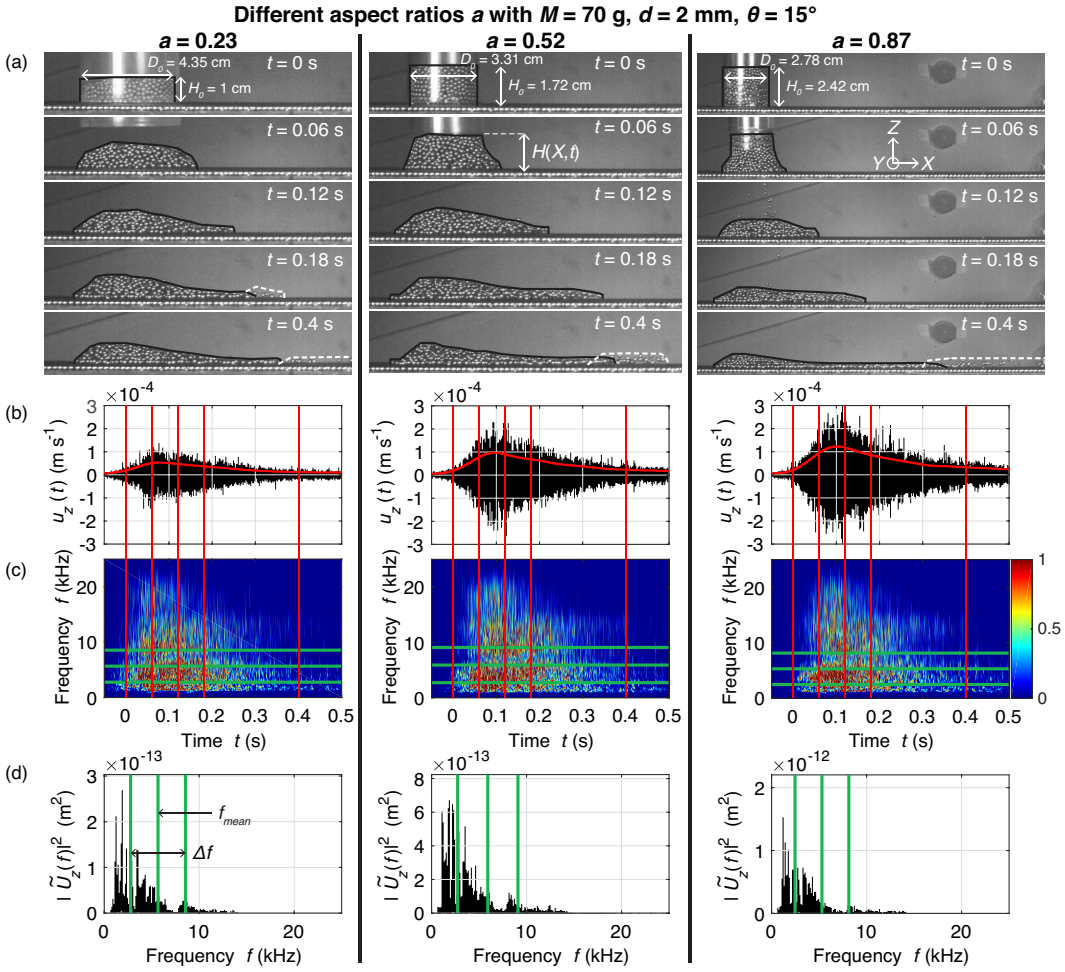


Figure B.2. Same as in Fig. B.1 but for slope angle $\theta = 15°$.

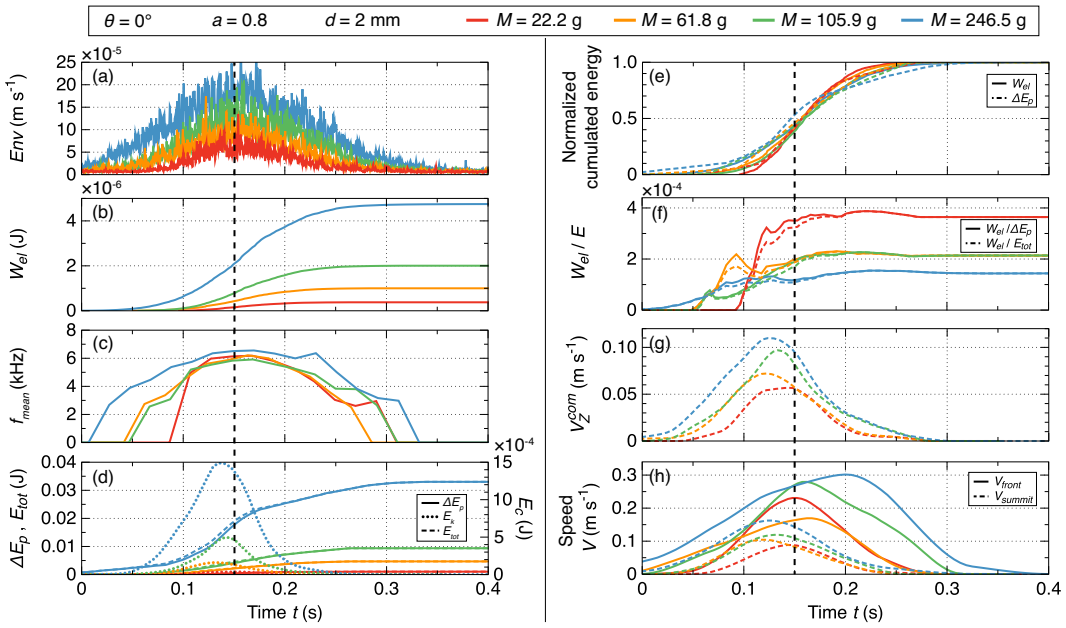


Figure B.3. Comparison of the dynamics of granular flows with the generated seismic signal for $\theta = 0°$, $a = 0.8$, $d = 2$ mm and different column masses M (different colors). (a) Envelope $Env(t)$ of the seismic signal filtered below 100 Hz. (b) Radiated seismic energy $W_{el}(t)$. (c) Mean frequency f_{mean}. (d) Potential energy lost ΔE_p, kinetic energy E_k and total energy $E_{tot} = \Delta E_p + E_k$. (e) Normalized cumulated radiated seismic energy $W_{el}(t)$ and potential energy lost ΔE_p. (f) Ratio of the radiated seismic energy over the potential energy lost and the total energy lost. (g) Speed V_Z^{COM} of the flow center-of-mass in the Z-direction. (h) Speed V_{front} and V_{summit} of the flow front (in X-direction) and of the flow summit (in Z-direction).

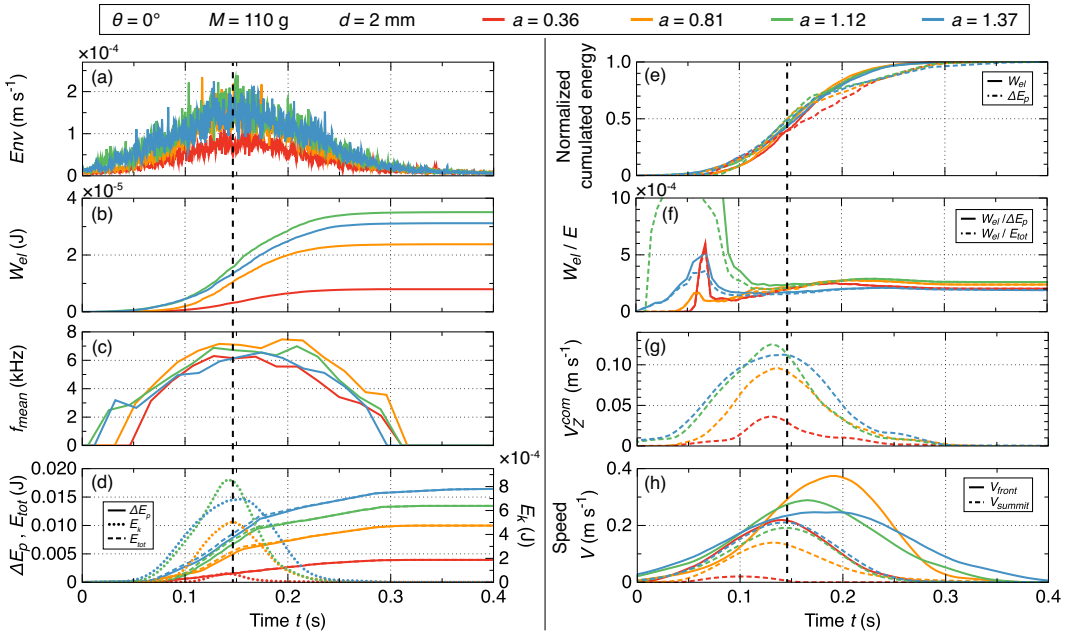


Figure B.4. Same as Fig. B.3 but for $\theta = 0°$, $M = 110$ g, $d = 2$ mm and different column initial aspect ratios a (different colors).

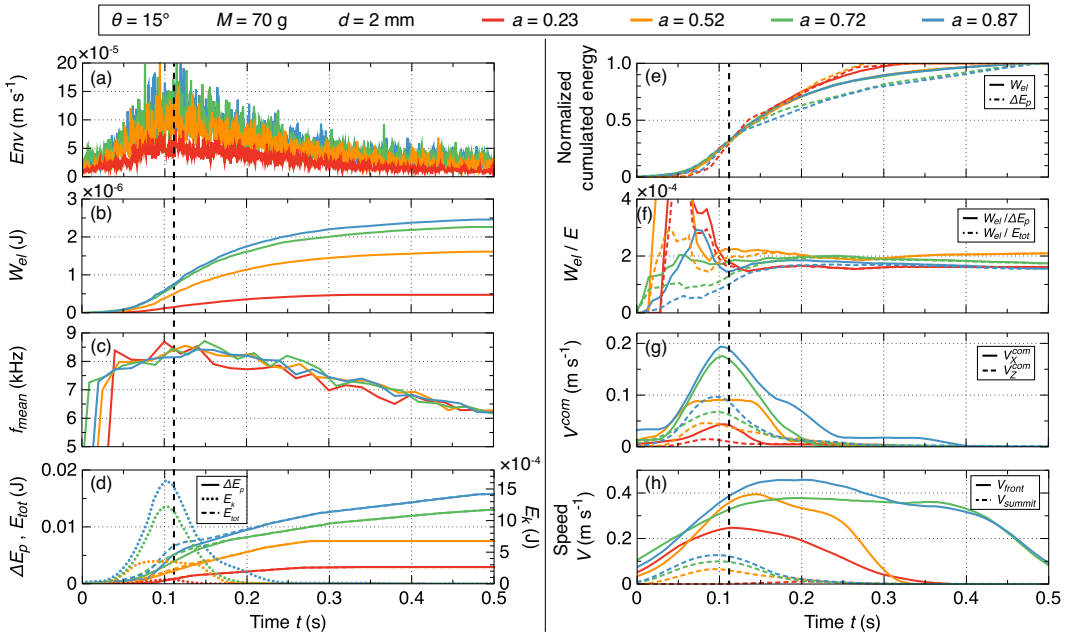


Figure B.5. Same as Fig. B.3 but for $\theta = 15°$, $M = 70$ g, $d = 2$ mm and different column initial aspect ratios a (different colors).

1048 **Table C.1.** Normalized scaling laws.

$$
\begin{array}{rcl}
 & & 160E_k'^{0.5} \\
 & & 88.2E_k'^{0.56} \\
W_{el}' & \approx & 1.7d'^3M'^{0.74}\max(V_{tot}^{COM})'^{0.94} \\
 & & 0.7d'^3M'^{0.73}\max(V_{front})'^{1.04} \\
\hline
W_{el}'/H_0'^2 & \approx & 0.48/(\tan\delta-\tan\theta)^2+6.07 \\
\hline
W_{el}' & \approx & 1.4d'^3H_0'^2\left(\frac{0.081}{(\tan\delta-\tan\theta)^2}+1\right) \\
\hline
\max(V_{tot}^{COM})' & \approx & 0.6\left(\frac{H_0'^2}{M'^{0.74}}\left(\frac{0.081}{(\tan\delta-\tan\theta)^2}+1\right)\right)^{\frac{1}{0.94}} \\
\max(V_{front})' & \approx & 2.3\left(\frac{H_0'^2}{M'^{0.73}}\left(\frac{0.081}{(\tan\delta-\tan\theta)^2}+1\right)\right)^{\frac{1}{1.04}} \\
\hline
d' & \approx & 2.77\cdot10^{25}(f_{mean}')^{-6.66} \\
a' & \approx & 0.014\left(\frac{W_{el}'}{E_k'}\right)^{-0.77} \\
M' & \approx & 1.6\left(\frac{W_{el}'}{d'^3\max(V_{front})'^{1.04}}\right)^{1.37} \\
M' & \approx & 0.48\left(\frac{W_{el}'}{d'^3\max(V_{tot}^{COM})'^{0.94}}\right)^{1.35}.
\end{array}
$$

Notation

$\boldsymbol{A_{max}}$ Maximum amplitude of the seismic signal (m s^{-1})

$\boldsymbol{a}$ Aspect ratio $a = H_0/D_0$ (-)

$\boldsymbol{D_0}$, $\boldsymbol{H_0}$ Initial diameter and thickness of the granular column (m)

$\boldsymbol{d}$ Bead diameter (m)

$\boldsymbol{\Delta E_p}$, $\boldsymbol{E_p}$, $\boldsymbol{E_k}$, $\boldsymbol{E_{tot}}$ Potential energy lost, potential energy, bulk kinetic energy and total energy lost (J)

$\boldsymbol{Env(t)}$ Amplitude envelope of the seismic signal (m s^{-1})

$\boldsymbol{f}$, $\boldsymbol{\omega}$ Frequency and angular frequency (s^{-1})

$\boldsymbol{f_{mean}}$ Mean frequency of the signal (Hz)

$\boldsymbol{g}$ Gravitational acceleration (m s^{-2})

$\boldsymbol{H(X,t)}$, $\boldsymbol{l(Z,t)}$ Thickness and length profiles of the flow contour in the $(X, Y = 0, Z)$ plane (m)

$\boldsymbol{h}$, $\boldsymbol{V_p}$ Thickness (m) and volume (m^3) of the plate

$\boldsymbol{I_{imp}}$ Impulse per particle impact (N s)

$\boldsymbol{M}$ Mass of the granular flow (kg)

$\boldsymbol{m}$ Mass of a particle (kg)

$\boldsymbol{R_{imp}}$ Rate of particle impact (s^{-1})

$\boldsymbol{r_f}$ Runout distance (m)

$\boldsymbol{t}$ Time (s)

$\boldsymbol{t_s}$, $\boldsymbol{t_f}$ Duration of the seismic signal and duration of the flow motion (s)

$\boldsymbol{u_Z}$, $\boldsymbol{a_Z}$ Normal vibration speed (m s^{-1}) and acceleration (m s^{-2}) of the plate surface

$\boldsymbol{\tilde{U}_Z}$ Time Fourier transform of u_Z (m s^{-1}/Hz)

$\boldsymbol{V}$ Flow volume (m^3)

$\boldsymbol{V_i^{COM}}$, $\boldsymbol{V_{tot}^{COM}}$ Speed of the center of mass in the i direction and total speed (m s^{-1})

$\boldsymbol{V_{front}}$, $\boldsymbol{V_{summit}}$ Speeds of the flow front and summit (m s^{-1})

$\boldsymbol{u_Z}$ Impact speed of individual particles in the Z-direction (m s^{-1})

$\boldsymbol{v_z}$ Impact speed (m s^{-1})

$\boldsymbol{W}$ Width of the granular flow in the Y-direction (m)

$\boldsymbol{W_{el}}$ Seismic energy radiated during the impact (J)

$\boldsymbol{X}$, $\boldsymbol{Y}$, $\boldsymbol{Z}$ Coordinates in the reference frame of the inclined plate (m)

$\boldsymbol{X^{COM}}$, $\boldsymbol{Z^{COM}}$ Coordinates of the flow center of mass in the X and Z-directions (m)

$\boldsymbol{X^{front}}$, $\boldsymbol{Z^{summit}}$ Coordinates of the flow front and flow maximum height in the X and Z-directions (m)

$\boldsymbol{\delta}$ Friction angle (°)

$\boldsymbol{\theta}$ Slope angle (°)

$\boldsymbol{\rho_p}$ Density of the plate (kg m^3)

$\boldsymbol{\tau}$, $\boldsymbol{\gamma}$ Characteristic time (s) and coefficient (1/m) of energy attenuation

$\boldsymbol{\tau_c}$ Characteristic duration of a granular flow (s)

Acknowledgments

This work was supported by the Agence Nationale de la Recherche ANR LANDQUAKES, REALISE, ITN FLOWTRANS and ERC Contract No. ERC-CG-2013-PE10-617472 SLIDEQUAKES. The data used in this paper can be found at the following address: .

References

Aki, K., and P. Richards (1980), *Quantitative Seismology : Theory and Methods*, vol. 1, W.H. Freeman.

Allstadt, K. (2013), Extracting source characteristics and dynamics of the August 2010 Mount Meager landslide from broadband seismograms, *J. Geophys. Res.*, *118*(3), 1472–1490, doi:10.1002/jgrf.20110.

Andreotti, B., Y. Forterre, and O. Pouliquen (2013), *Granular Media: Between Fluid and Solid, vol. 1*, Cambridge Univ. Press.

Arattano, M. (2000), On Debris Flow Front Evolution Along a Torrent, *Phys. Chem. Earth (B)*, *25*(9), 733–740, doi:10.1016/S1464-1909(00)00094-0.

Arattano, M., and F. Moia (1999), Monitoring the propagation of a debris flow along a torrent, *Hydrol. Sci. J.*, *44*, 811–823, doi:10.1080/02626669909492275.

Arattano, M., and L. Marchi (2005), Measurements of debris flow velocity through cross-correlation of instrumentation data, *Natural Hazards and Earth System Sciences*, *5*, 137–142.

Bachelet, V., A. Mangeney, R. Toussaint, and J. de Rosny (2017), Seismic signal of near steady uniform flows, *AGU Fall Meeting*.

Bachelet, V., A. Mangeney, J. De Rosny, R. Toussaint, and M. Farin (2018a), Elastic wave generated by granular impact on rough and erodible surfaces, *J. Applied*

Phys., *123*, 044,901, doi:10.1063/1.5012979.

Bachelet, V., A. Mangeney, R. Toussaint, and J. de Rosny (2018b), Which dynamic properties can be recovered from the seismic signal of steady and uniform granular flows ?, *EGU General Assembly*.

Balmforth, N. J., and R. R. Kerswell (2005), Granular collapse in two dimensions, *J. Fluid Mech.*, *538*(1), 399–428, doi:10.1017/S0022112005005537.

Barrière, J., A. Krein, A. Oth, and R. Schenkluhn (2015), An advanced signal processing technique for deriving grain size information of bedload transport from impact plate vibration measurements, *Earth Surf. Process. Landforms*, *40*, 913–924, doi:10.1002/esp.3693.

Brodsky, E., E. Gordeev, and H. Kanamori (2003), Landslide basal friction as measured by seismic waves, *Geophys. Res. Lett.*, *30*(24), 2236, doi:10.1029/2003GL018485.

Burtin, A., L. Bollinger, R. Cattin, J. Vergne, and J. L. Nábělek (2009), Spatiotemporal sequence of Himalayan debris flow from analysis of high-frequency seismic noise, *J. Geophys. Res.*, *114*(F4), F04,009.

Burtin, A., J. Vergne, L. Rivera, and P. Dubernet (2010), Location of river-induced seismic signal from noise correlation functions, *Geophys. J. Int.*, *182*(3), 1161–1173.

Dammeier, F., J. R. Moore, F. Haslinger, and S. Loew (2011), Characterization of alpine rockslides using statistical analysis of seismic signals, *J. Geophys. Res.*, *116*(F4), F04,024, doi:10.1029/2011JF002037.

Delannay, R., A. Valance, A. Mangeney, O. Roche, and P. Richard (2017), Granular and particle-laden flows: from laboratory experiments to field observations, *Journal of Physics D: Applied Physics*, *50*(5), 053,001, doi:10.1088/1361-6463/50/5/053001.

Deparis, J., D. Jongmans, F. Cotton, L. Baillet, F. Thouvenot, and D. Hantz (2008), Analysis of rock-fall and rock-fall avalanche seismograms in the French Alps, *Bull. Seism. Soc. Am.*, *98*(4), 1781–1796, doi:10.1785/0120070082.

Ekström, G., and C. P. Stark (2013), Simple Scaling of Catastrophic Landslide Dynamics, *Science*, *339*(6126), 1416–1419.

Farin, M., A. Mangeney, and O. Roche (2014), Fundamental changes of granular flow dynamics, deposition, and erosion processes at high slope angles:

Insights from laboratory experiments, *J. Geophys. Res.*, *119*, 504–532, doi:10.1002/2013JF002750.

Farin, M., A. Mangeney, R. Toussaint, J. de Rosny, N. Shapiro, T. Dewez, C. Hibert, C. Mathon, O. Sedan, and F. Berger (2015), Characterization of rockfalls from seismic signal: Insights from laboratory experiments, *J. Geophys. Res.*, *120*, doi:10.1002/2015JB012331.

Farin, M., A. Mangeney, J. de Rosny, R. Toussaint, J. Sainte-Marie, and N. Shapiro (2016), Experimental validation of theoretical methods to estimate the energy radiated by elastic waves during an impact, *J. Sound Vib.*, *362*, 176–202, doi:10.1016/j.jsv.2015.10.003.

Farin, M., A. Mangeney, J. de Rosny, R. Toussaint, and T. Phuong-Thu (2018), Link Between the Dynamics of Granular Flows and the Generated Seismic Signal: Insights From Laboratory Experiments, *J. Geophys. Res.: Earth Surface*, *123*, doi:10.1029/2017JF004296.

Farin, M., V. Tsai, M. Lamb, and K. Allstadt (2019), A physical model for the high-frequency seismic signal generated by debris flows, *Earth Surf. Process. Landforms*, doi:10.1002/esp.4677.

Favreau, P., A. Mangeney, A. Lucas, G. Crosta, and F. Bouchut (2010), Numerical modeling of landquakes, *Geophys. Res. Let.*, *37*, L15,305, doi:10.1029/2010GL043512.

GdR Midi (2004), On dense granular flows, *Eur. Phys. J. E*, *14*(4), 341–365, doi:10.1140/epje/i2003-10153-0.

Helmstetter, A., and S. Garambois (2010), Seismic monitoring of Séchilienne rockslide (French Alps): Analysis of seismic signals and their correlation with rainfalls, *J. Geophys. Res.*, *115*, F03,016, doi:10.1029/2009JF001532.

Hibert, C., A. Mangeney, G. Grandjean, and N. M. Shapiro (2011), Slope instabilities in Dolomieu crater, Réunion Island: From seismic signals to rockfall characteristics, *J. Geophys. Res.*, *116*, F04,032, doi:10.1029/2011JF002038.

Hibert, C., G. Ekström, and C. Stark (2014a), Dynamics of the Bingham Canyon Mine landslides from seismic signal analysis, *Geophys. Res. Lett.*, *41*, 4535–4541, doi:10.1002/2014GL060592.

Hibert, C., A. Mangeney, G. Grandjean, C. Baillard, D. Rivet, N. M. Shapiro, C. Satriano, A. Maggi, P. Boissier, V. Ferrazzini, and W. Crawford (2014b), Automated

identification, location, and volume estimation of rockfalls at piton de la fournaise volcano, *J. Geophys. Res.*, *119*(5), 1082–1105, doi:10.1002/2013JF002970.

Hibert, C., G. Ekström, and C. P. Stark (2017a), The relationship between bulk-mass momentum and short-period seismic radiation in catastrophic landslides, *J. Geophys. Res.*, *122*, 1201–1215, doi:10.1002/2016JF004027.

Hibert, C., A. Mangeney, G. Grandjean, A. Peltier, A. DiMuro, N. Shapiro, V. Ferrazzini, P. Boissier, V. Durand, and P. Kowalski (2017b), Spatio-temporal evolution of rockfall activity from 2007 to 2011 at the Piton de la Fournaise volcano inferred from seismic data, *J. Volcano. Geotherm. Res.*, *333–334*, 36–52, doi:10.1016/j.jvolgeores.2017.01.007.

Hibert, C., J. Malet, F. Bourrier, F. Provost, F. Berger, P. Bornemann, P. Tardiff, and E. Mermin (2017c), Single-block rockfall dynamics inferred from seismic signal analysis, *Earth Surf. Dynam.*, *5*, 283–292, doi:10.5194/esurf-5-283-2017.

Hogg, A. J. (2007), Two-dimensional granular slumps down slopes, *Phys. Fluids*, *19*, 093,301, doi:10.1063/1.2762254.

Hsu, L., W. E. Dietrich, and L. S. Sklar (2014), Mean and fluctuating basal forces generated by granular flows: Laboratory observations in a large vertically rotating drum, *J. Geophys. Res.*, *119*(6), 1283–1309, doi:10.1002/2013JF003078.

Huang, C.-J., C.-L. Shieh, and H.-Y. Yin (2004), Laboratory study of the underground sound generated by debris flows, *J. Geophys. Res.*, *109*(F1), doi:10.1029/2003JF000048.

Huang, C.-J., H.-Y. Yin, C.-Y. Chen, C.-H. Yeh, and C.-L. Wang (2007), Ground vibrations produced by rock motions and debris flows, *J. Geophys. Res.*, *112*(F02014), doi:10.1029/2005JF000437.

Iverson, R. (1997), The physics of debris flows, *Reviews of Geophysics*, *35*, 245–296, doi:10.1029/97RG00426.

Kean, J., J. Coe, V. Coviello, J. Smith, S. McCoy, and M. Arattano (2015), Estimating rates of debris flow entrainment from ground vibrations, *J. Geophys. Res.*, *42*, doi:10.1002/ 2015GL064811.

Lai, V., V. Tsai, M. Lamb, T. Ulizio, and A. Beer (2018), The Seismic Signature of Debris Flows: Flow Mechanics and Early Warning at Montecito, California, *Geophys. Res. Let.*, *45*, 5528–5535, doi:10.1029/2018GL077683.

Lévy, C., A. Mangeney, F. Bonilla, C. Hibert, E. Calder, P. Smith, and P. Cole (2015), Friction weakening in granular flows deduced from seismic records at the Souffrière Hills Volcano, Montserrat, *J. Geophys. Res.*, *120*, 7536–7557, doi: 10.1002/2015JB012151.

Lube, G., H. E. Huppert, R. S. J. Sparks, and A. Freundt (2005), Collapses of two-dimensional granular columns, *Phys. Rev. E*, *72*(4), 041,301, doi: 10.1103/PhysRevE.72.041301.

Lube, G., H. E. Huppert, R. S. J. Sparks, and A. Freundt (2011), Granular column collapses down rough, inclined channels, *J. Fluid Mech.*, *675*, 347–368, doi: 10.1017/jfm.2011.21.

Mangeney, A., O. Roche, O. Hungr, N. Mangold, G. Faccanoni, and A. Lucas (2010), Erosion and mobility in granular collapse over sloping beds, *J. Geophys. Res.*, *115*(F3), F03,040, doi:10.1029/2009JF001462.

Moretti, L., A. Mangeney, Y. Capdeville, E. Stutzmann, C. Huggel, D. Schneider, and F. Bouchut (2012), Numerical modeling of the Mount Steller landslide flow history and of the generated long period seismic waves, *Geophys. Res. Lett.*, *39*(16), doi:10.1029/2012GL052511.

Moretti, L., K. Allstadt, A. Mangeney, Y. Capdeville, E. Stutzmann, and F. Bouchut (2015), Numerical modeling of the Mount Meager landslide constrained by its force history derived from seismic data, *J. Geophys. Res.*, *120*, 2579–2599, doi:10.1002/2014JB011426.

Norris, R. D. (1994), Seismicity of rockfalls and avalanches at three cascade range volcanoes: Implications for seismic detection of hazardous mass movements, *Bull. Seism. Soc. Am.*, *84*(6), 1925–1939.

Pérez-Guillén, C., B. Sovilla, E. Suriñach, M. Tapiac, and A. Köhler (2016), Deducing avalanche size and flow regimes from seismic measurements, *Cold Regions Science and Technology*, *121*, 25 – 41, doi:10.1016/j.coldregions.2015.10.004.

Royer, D., and E. Dieulesaint (2000), *Elastic Waves in Solids I: Free and Guided Propagation*, Springer.

Schneider, D., P. Bartelt, J. Caplan-Auerbach, M. Christen, C. Huggel, and B. W. McArdell (2010), Insights into rock-ice avalanche dynamics by combined analysis of seismic recordings and a numerical avalanche model, *J. Geophys. Res.*, *115*(F4), F04,026, doi:10.1029/2010JF001734.

Siavoshi, S., and A. Kudrolli (2005), Failure of a granular step, *Phys. Rev. E*, *71*(5), 051,302, doi:10.1103/PhysRevE.71.051302.

Suriñach, E., I. Vilajosana, G. Khazaradze, B. Biescas, G. Furdada, and J. M. Vilaplana (2005), Seismic detection and characterization of landslides and other mass movements, *Nat. Hazards Earth Syst. Sci.*, *5*(6), 791–798, doi:10.5194/nhess-5-791-2005.

Taylor, S., and E. Brodsky (2017), Granular temperature measured experimentally in a shear flow by acoustic energy, *Phys. Rev. E.*, *96*, 032,913.

Turkaya, S., R. Toussaint, F. Eriksen, M. Zecevic, G. Daniel, E. Flekky, and K. J. Mly (2015), Bridging aero-fracture evolution with the characteristics of the acoustic emissions in a porous medium, *Frontiers in Physics*, *3*, 70, doi:10.3389/fphy.2015.00070.

Turquet, A., R. Toussaint, F. Eriksen, G. Daniel, D. Koehn, and E. Flekky (2018), Microseismic emissions during pneumatic fracturing: A numerical model to explain the experiments, *Journal of Geophysical Research: Solid Earth*, *123*(8), 6922–6939, doi:10.1029/2017JB014613.

Turquet, A., R. Toussaint, F. Eriksen, G. Daniel, O. Lenglin, E. Flekky, and K. Mly (2019), Source localization of microseismic emissions during pneumatic fracturing, *Geophysical Research Letters*, *46*(7), 3726–3733, doi:10.1029/2019GL082198.

Vilajosana, I., E. Suriñach, A. Abellan, G. Khazaradze, D. Garcia, and J. Llosa (2008), Rockfall induced seismic signals: case study in Montserrat, Catalonia, *Nat. Hazards Earth Syst. Sci.*, *8*(4), 805–812, doi:10.5194/nhess-8-805-2008.

Yamada, M., Y. Matsushi, M. Chigira, and J. Mori (2012), Seismic recordings of landslides caused by Typhoon Talas (2011), Japan, *Geophys. Res. Lett.*, *39*(13), doi:10.1029/2012GL052174.

Yamada, M., A. Mangeney, Y. Matsushi, and L. Moretti (2016), Estimation of dynamic friction process of the Akatani landslide based on the waveform inversion and numerical simulation, *Geophys. J. Int.*, *206*, 1479–1486, doi:10.1093/gji/ggw216.

Yamada, M., A. Mangeney, Y. Matsushi, and T. Matsuzawa (2018), Estimation of dynamics friction and movement history of large landslides, *Landslides*, doi:10.1007/s10346-018-1002-4.

Yohannes, B., L. Hsu, W. Dietrich, and K. Hill (2012), Boundary stresses due to impacts from dry granular flows, *J. Geophys. Res.*, *117*, F02,027.

Zhao, J., L. Moretti, A. Mangeney, E. Stutzmann, H. Kanamori, Y. Capdeville, E. Calder, C. Hibert, P. Smith, P. Cole, and A. LeFriant (2015), Model space exploration for determining landslide source history from long-period seismic data, *Pure Appl. Geophys.*, *172*(2), 389–413, doi:10.1007/s00024-014-0852-5.